



HAL
open science

The plume head-lithosphere interaction using a tectonically realistic formulation for the lithosphere

Evgenii E.B. Burov, Laurent Guillou-Frottier

► **To cite this version:**

Evgenii E.B. Burov, Laurent Guillou-Frottier. The plume head-lithosphere interaction using a tectonically realistic formulation for the lithosphere. *Geophysical Journal International*, 2005, 161 (2), pp.469-490. 10.1111/j.1365-246X.2005.02588.x . hal-00023754

HAL Id: hal-00023754

<https://hal.science/hal-00023754>

Submitted on 1 Mar 2021

HAL is a multi-disciplinary open access archive for the deposit and dissemination of scientific research documents, whether they are published or not. The documents may come from teaching and research institutions in France or abroad, or from public or private research centers.

L'archive ouverte pluridisciplinaire **HAL**, est destinée au dépôt et à la diffusion de documents scientifiques de niveau recherche, publiés ou non, émanant des établissements d'enseignement et de recherche français ou étrangers, des laboratoires publics ou privés.

The plume head–continental lithosphere interaction using a tectonically realistic formulation for the lithosphere

E. Burov¹ and L. Guillou-Frottier²

¹Laboratoire de Tectonique, Université Pierre & Marie Curie, Paris, France. E-mail: evgenii.burov@lgs.jussieu.fr

²Service des Ressources Minérales, Bureau de Recherches Géologiques et Minières, Orléans, France. E-mail: l.guillou-frottier@brgm.fr

Accepted 2005 January 18. Received 2004 December 9; in original form 2004 July 8

SUMMARY

Current debates on the existence of mantle plumes largely originate from interpretations of supposed signatures of plume-induced surface topography that are compared with predictions of geodynamic models of plume–lithosphere interactions. These models often inaccurately predict surface evolution: in general, they assume a fixed upper surface and consider the lithosphere as a single viscous layer. In nature, the surface evolution is affected by the elastic–brittle–ductile deformation, by a free upper surface and by the layered structure of the lithosphere. We make a step towards reconciling mantle- and tectonic-scale studies by introducing a tectonically realistic continental plate model in large-scale plume–lithosphere interaction. This model includes (i) a natural free surface boundary condition, (ii) an explicit elastic–viscous(ductile)–plastic(brittle) rheology and (iii) a stratified structure of continental lithosphere. The numerical experiments demonstrate a number of important differences from predictions of conventional models. In particular, this relates to plate bending, mechanical decoupling of crustal and mantle layers and tension–compression instabilities, which produce transient topographic signatures such as uplift and subsidence at large (>500 km) and small scale (300–400, 200–300 and 50–100 km). The mantle plumes do not necessarily produce detectable large-scale topographic highs but often generate only alternating small-scale surface features that could otherwise be attributed to regional tectonics. A single large-wavelength deformation, predicted by conventional models, develops only for a very cold and thick lithosphere. Distinct topographic wavelengths or temporarily spaced events observed in the East African rift system, as well as over French Massif Central, can be explained by a single plume impinging at the base of the continental lithosphere, without evoking complex asthenospheric upwelling.

Key words: geodynamics, lithospheric deformation, mantle plume, numerical techniques, rheology, topography.

1 INTRODUCTION

Theories and models of thermal convection in the mantle of the Earth suggest the existence of plumes of hot material that may rise from deep levels. Among various possible shapes of upwellings within a convecting medium, the mantle plume is a gigantic diapir, which comprises a narrow tail and a large spherical or mushroom-shaped head. This concept explains a number of geological observations at the surface, as well as convection driven by cooling of the core of the Earth (Davies 1993; Jellinek & Manga 2004). Nevertheless, more direct seismic evidences for mantle plumes would require imaging at higher resolution than has been available (e.g. Sleep 2004 but see, however, Montelli *et al.* 2004). For this reason, a number of recent studies have triggered a new debate on the validity of the mantle plume concept (Sheth 1999; Foulger 2002) and on the possible different explanations for surface signatures com-

monly associated with mantle plumes (Anderson 1998; Courtillot *et al.* 1999; Ingle & Coffin 2004). Most arguments against the mantle plume concept are based on a confrontation between observations, and theoretical and modelling predictions for geochemical and geophysical consequences of the interaction between the plume head and the overlying lithosphere. However, these predictions depend on the degree of reality in plume–lithosphere interaction models, which are often designed to reproduce deep mantle dynamics and consider a highly simplified lithosphere. In most (yet not all) of them, the lithosphere is a stagnant viscous lid with a fixed surface. This naturally does not permit for direct prediction of surface and intralithosphere deformation, as well as of a host of plate-scale tectonic and geological consequences of plume–lithosphere interactions. For this reason, it may appear that some of the criticisms of the plume concept address the models rather than plumes themselves.

In recent decades, laboratory experiments on mantle convection have shown that in laboratory conditions, several upwelling geometries could be obtained, depending on viscosity and density contrasts (e.g. Griffiths & Campbell 1990). Numerical modelling allows inclusion of additional effects that cannot be reproduced in the laboratory. However, after almost three decades of modelling of mantle plumes by all possible techniques, the fate of the plume head making contact with the lithosphere has scarcely been tackled in terms of its consequences for plate and crustal dynamics. Among the geophysical signatures associated with mantle plumes, high mantle temperatures, surface uplift and thermal erosion of the lithosphere constitute the principal arguments for their existence. Yet, these features are only approximately reproduced in large-scale numerical models that include a single viscous layer for the lithosphere and fixed upper boundary conditions (e.g. Sleep 2003). Moreover, most of the studies are focused on the impingement of mantle plumes on oceanic lithosphere (e.g. Olson 1990; Ribe & Christensen 1994), which dramatically differs, in terms of its mechanical properties, from the continental lithosphere (Burov & Diament 1995). Even in the oceanic domain, only a few models exist that account for a natural free surface boundary condition and the rheological structure of the lithosphere (d'Acremont *et al.* 2003). The present study extends the latter approach to the continental domain, which requires accounting for elastic, ductile and brittle properties of the continental lithosphere referred to as elastic–viscous–plastic (EVP) rheology. One of the objectives of this work is to show that both the surface signatures associated with plume–continental lithosphere interaction and the thermomechanical processes in the deep lithosphere are more complex and tectonically more relevant than the signatures predicted from studies with a simplified lithosphere. Our study focuses on the physical processes of plume head impingement at the base of the lithosphere, with particular emphasis on plume head flattening, thermomechanical erosion and the mechanical responses of the lithosphere. Predicted surface topographies are outlined and used to interpret uplift and subsidence in terms of me-

chanical coupling/uncoupling between different rheological layers within the lithosphere. This study is mainly devoted to the general processes and physics of the plume–lithosphere interactions. A preliminary comparison between modelling results and surface topography in East Africa is also presented.

2 SUBCONTINENTAL MANTLE PLUMES AND CONTINENTAL LITHOSPHERE

Although a number of studies reject the existence of mantle plumes, simple physical arguments can be invoked to justify the ascent of hot material below the continental lithosphere from the base of the mantle. The heterogeneous upper surface of the mantle has been shown to represent a mixed thermal condition, between a fixed temperature condition imposed below the oceanic domain and a constant heat flow condition, which develops below the continental domain. In general, a heterogeneous thermal condition has major dynamic consequences in thermal convection (Chapman *et al.* 1980), such as modifying stable wavelengths for convection or changing thermal budget. The presence of buoyant continents at the top of the convecting mantle maintains a non-imposed thermal condition, which evolves towards a near-constant and low heat flow condition as soon as the continental area is large enough (Guillou & Jaupart 1995). This insulating behaviour of continents (e.g. Anderson 1982) has been confirmed by measurements of terrestrial heat flow (Kukkonen & Peltonen 1999; Mareschal *et al.* 1999). As a result of the low mantle heat flow beneath continents, temperatures in the subcontinental regions are higher than those beneath the oceanic regions and the resulting lateral temperature gradients induce mantle flow from the subcontinental domains towards the suboceanic mantle. It follows that the ascent of hot material is favoured beneath the centre of the continent, thus initiating a mantle plume (Fig. 1a). Laboratory (Fig. 1b; Guillou & Jaupart 1995) and numerical experiments (e.g. Lenardic *et al.* 2000) have confirmed that heterogeneous

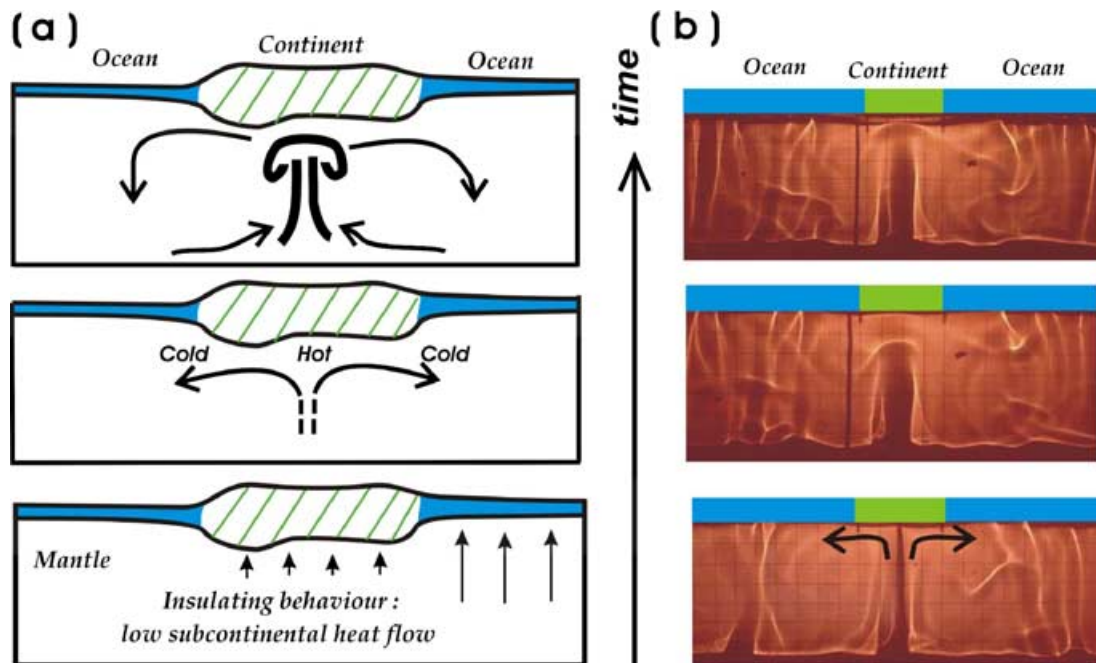


Figure 1. Possible mechanisms and consequences of the emplacement of mantle plumes below continents. (a) Low subcontinental mantle heat flow triggers lateral temperature gradients that induce horizontal mantle flow from the continental towards oceanic domain; the resulting vertical mantle flow gives rise to a subcontinental mantle plume. (b) Snapshot of the analogue experiment that reproduced this mechanism (Guillou & Jaupart 1995).

thermal conditions at the top of the convecting mantle result in formation of subcontinental mantle plumes, embedded in suboceanic downwellings.

A large number of geodynamic observations support the mantle plume concept below continents. The episodic character of continental growth, as revealed by distribution of juvenile continental crust (McCulloch & Bennett 1994), is supposed to be related to catastrophic superplume events in the mantle (Condie 2002). Periods of supercontinent formation, periods of identified metallogenic crises and/or periods of intense magmatism can also be related to enhanced mantle plume activity. Various geological records, such as those described by Condie *et al.* (2000), may be closely associated with mantle (super)plume events.

It is now well established that deep dynamic processes affect crustal behaviour. This behaviour is largely conditioned by brittle–elastic properties of the crust and of the underlying lithosphere rather than by viscous properties of the deeper mantle. The geological observations of crustal deformation present one of the main sources of information on the tectonic history of the lithospheric plates. For this reason, any study of dynamics of plume–lithosphere interaction must realistically reproduce thermomechanical conditions in the lithosphere when a mantle plume impinges at its base. This requires accounting for brittle–elastic–ductile lithosphere with a layered structure reflecting highly contrasting properties of the continental crust and mantle (density, rheology, heat production).

In contrast to the oceanic lithosphere that behaves as a single mechanical layer, the continental lithosphere is composed of mechanically decoupled layers that include the upper, intermediate and lower crust and the mantle part (e.g. Burov & Diament 1995; Burov & Poliakov 2001). Compared with single layers, the mechanics of multilayers presents numerous surprises, specifically in the case of large strain—large amplitude deformation (e.g. Gerbault *et al.* 1998). For example, deformation of different layers may correlate, miscorrelate or destructively interfere with each other resulting in multiharmonic or even chaotic surface deformation and in alternating movements at the surface (e.g. Hunt *et al.* 1996). As a result of the multilayered structure of the continental lithosphere (detailed in Section 3.2), one can expect significant differences in the surface expression of plume–lithosphere interactions, because of a possible decoupling between the crust and mantle. Such decoupling (together with the free surface boundary condition) may result in series of subsiding and uplifting regions, as well as in extensional and compressional instabilities. Plume–lithosphere interactions beneath an elastic–ductile–brittle oceanic lithosphere with free upper surface have already been described in our previous paper (d’Acremont *et al.* 2003). This study has shown that the free surface boundary condition allows for more degrees of freedom than the conventional approach. As a result, ups and downs and series of compression/extension zones were predicted at the surface. In addition, the predicted amplitudes and wavelengths of deformation also reveal a number of differences from fixed-surface models.

The problem of plume initiation was thoroughly examined in previous studies and, for this reason, we focus our experiments on different modes of plume–lithosphere interactions and consider different thermal and rheological structures of the continental lithosphere. Similarly, physical processes triggering a mantle plume event, such as thermal conditions described in Fig. 1(a), are not considered. In order to compare our results with analogous studies for the oceanic plates (d’Acremont *et al.* 2003), we first consider a monolayer continental lithosphere. Then, we introduce a multilayer crust–mantle structure. Plume dynamics are parametrized by a plume Rayleigh

number derived from commonly inferred temperature and density contrasts.

Before giving a detailed description of the numerical experiments and their results, we find it necessary to list all previous hypotheses that were commonly used in studies on plume–lithosphere interactions, in order to stress the novelty of our approach. The following Section 3 thus provides a review of previous assumptions and gives additional information on the realistic approach used in our study.

3 COMMON ASSUMPTIONS OF PLUME MODELS

3.1 Mantle rheology

In addition to tectonically oversimplified representation of the lithosphere by a viscous lid (see Section 3.2), the asthenospheric and mantle material is often considered to have constant, linearly varying, or temperature-dependent Newtonian viscosity (e.g. Loper & Stacey 1983). Resulting models yield plume ascent rates on the order of 0.2 to 2 m yr⁻¹, predicting that plumes should lose a large amount of their thermal energy during their ascent. This implies the formation of large-scale blurred zones (haloes) of thermal influence at depth, originating from extensive heat diffusion from a slow plume. Later studies of diapirism (Weinberg & Podladchikov 1994; Van Keken 1997; d’Acremont *et al.* 2003; Burov *et al.* 2003) demonstrated that ascent rates might be several orders of magnitude higher (hundreds and thousands of m yr⁻¹) in cases of non-Newtonian power-law viscosity. Such a rapid ascent results in a reduced size of the critical thermal layer around the head and tail of the diapir, and in essentially higher thermomechanical potential of the diapir when it arrives at the surface. The continental plates migrate at rates 5–10 times slower than those of oceanic plates. With slow plates and high plume ascent rates, there is no need to account for horizontal plate motions in plume–continental lithosphere interactions and no hotspot tracks are expected.

Fast ascent of hot material is expected to modify rheological properties of the mantle lithosphere and thus its mechanical response. On the one hand, thermal energy stored in the plume head is sufficient to reduce the viscosity of the lower part of the lithosphere. On the other hand, the fast ascent of the plume should promote brittle faulting and horizontal intraplate instabilities in response to the impact of the plume head. The analytical and numerical estimates of plume dynamics appear to be approximate, in particular as a result of the strong dependence of the results on temperature and rheological assumptions (Sleep 1997, 2002, 2003). Consequently, it is difficult to compare or to test models on the basis of previously estimated ascent rates, which justifies a new numerical approach.

3.2 Lithosphere rheology

The lithosphere deformation is dominated by elastoplastic and elastoviscous–plastic behaviour in the crust and uppermost mantle (Figs 2a and b). Until recently, the plume–lithosphere interactions were tackled within the hydrodynamic approach based on the solution of viscous flow equations (e.g. Ribe & Christensen 1994; Doin *et al.* 1997; Sleep 1997; Solomatov & Moresi 2000; Tackley 2000). Most models of plume ascent considered the lithosphere as a stagnant viscous lid with a fixed surface. Instead, lithospheric-scale studies show that the lithosphere behaves as an elastic–brittle–ductile multilayer, whose mechanical response involves flexural bending, pure and simple shear, localized brittle deformation, compressional

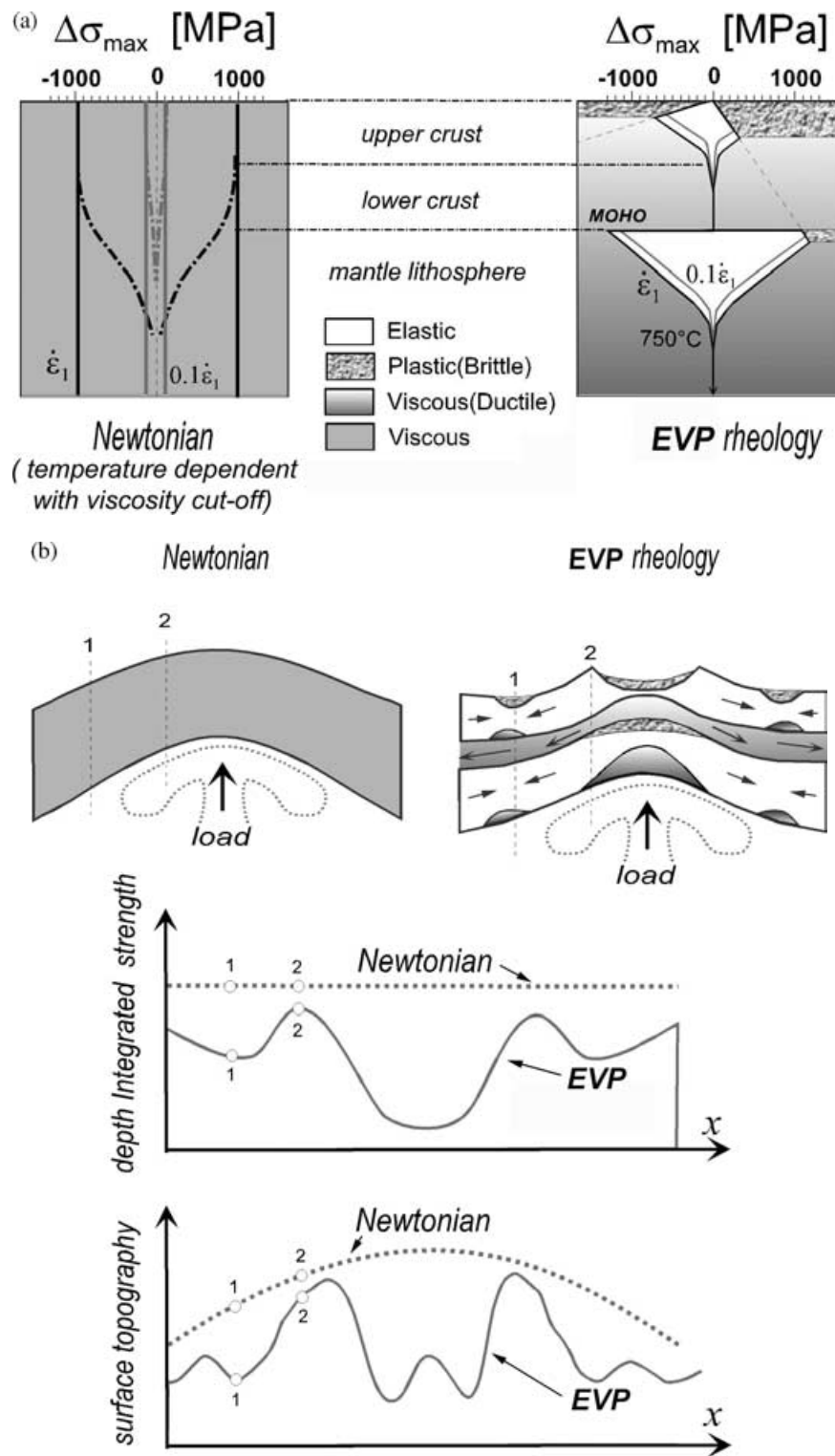


Figure 2. (a) Comparison of vertical strength profiles for viscous Newtonian rheology used in common models (left, viscosity at top = 10^{24} Pa s) and (right) continental rheology EVP with quartz-dominated crust (thermal age of 150 Ma, Tables 1 and 2). Dashed lines correspond to temperature-dependent Newtonian viscosity. Shown are maximal shear stresses for two fixed strain rates ($\partial\epsilon_1/\partial x = 10^{-15} \text{ s}^{-1}$, black contours) and $(0.1\partial\epsilon_1/\partial x)$, grey contours). For non-Newtonian constitutive relationships (quartz, diabase, olivine), stress dependence on strain rate is approximately 10 times smaller than for Newtonian viscosity. In the case of continental EVP rheology, crust is mechanically decoupled from the mantle; stresses cannot grow over yield stress limits, which results in a local reduction of integrated plate strength. (b) Comparison of plate behaviour in the cases of Newtonian and EVP rheology (modified from Burov & Poliakov 2001). For EVP rheology, brittle and ductile failure in regions of maximum deformation (e.g. bending) result in local weakening and strain localization (top, right); large periodic variations of integrated strength ($\int_z \sigma(z) dz$, middle) result from alternation of flexural strain in the lithosphere, thus creating a feedback between strength and strain. Bottom: comparison of surface behaviour for linear and EVP rheology schematized as the convolution between the integrated strength of the plate and plume-induced basal topography; lithosphere modulates deformation caused by a plume.

or tensional instabilities (Burov & Poliakov 2001; Burov *et al.* 2001; Frederiksen & Braun 2001). As demonstrated in Fig. 2(b), a plume may produce two major effects on the lithosphere: necking and boudinage as a result of background extension caused by plume spreading; and flexural response as a result of plume loading normal to the lithosphere. Both result in periodically varying integrated strength of the plate measured in terms the equivalent elastic thickness (EET) of the lithosphere (e.g. Burov & Diament 1995; Turcotte & Schubert 2002). In the case of EVP rheology, the integrated strength becomes laterally variable, which enhances localization of deformation and thus variations of topography, leading to the establishment of a feedback between strength, surface and subsurface deformation. Such a system would have little to do with a viscous lid. However, plume models still use the viscous or pseudo-viscous lid concept even to reproduce non-viscous deformation (e.g. Bercovici *et al.* 2001; Solomatov 2001). Yet, the approximation of non-viscous behaviour by the viscous or pseudo-viscous approach is limited: viscous rheology remains distinct from elasticity and plasticity as it relates stress to strain rate, while both brittle or elastic behaviour are generally strain-rate independent (Byerlee 1978; Turcotte & Schubert 2002).

3.3 Viscous versus non-viscous rheology: introducing an explicit approach used for tectonic modelling

Correct accounting for non-viscous rheology requires a mechanical approach that is not limited to flow. In particular, accounting for plasto-elastic rheology requires the computation of total and accumulated strain and total (including static) pressure that are not explicitly present in flow equations. This problem is circumvented by solving more general Newton's equations of motion (Appendix A) instead of flow equations. The constitutive laws for EVP rheology correspond to a serial (Maxwell type) body:

$$\varepsilon_{ij} = \varepsilon_{ije} + \varepsilon_{ijv} + \varepsilon_{ijp}, \quad (1)$$

where ε_{ij} stands for the components of strain tensor and subscripts e, v, p refer respectively to elastic, viscous and plastic contributions to total strain (see Appendix B). Eq. (1) is solved in incremental form, which provides control of both strains and strain rates. The total strain increment is defined by a sum of elastic, plastic (brittle) and viscous (ductile) strain increments. Each strain increment is computed according to its constitutive law, or rheological term. We use linear elastic, Mohr–Coulomb plastic and non-linear power-law ductile creep rheological terms (Appendices A and B). In the present formulation, we apply a modified form of the eq. (1), in which the total strain increment is defined for each numerical element depending on which rheological couple, elastic–plastic or elastic–viscous, provides the smaller stress. This substitution is justified for short time steps used in our experiments (large Deborah number, i.e. large ratio of relaxation time to time step). This assumption is well suited for conditions of the real Earth, where one behaviour, elastoplastic or viscoelastic, almost always dominates the other (e.g. Goetze & Evans 1979).

Two notions of the effective viscosity can be associated with the eq. (1). The first notion relates to the true effective viscosity of the viscous–ductile part, determined as

$$\mu_{\text{eff}} = \tau^{\text{II}} / \partial \varepsilon_v^{\text{II}} / \partial t, \quad (2)$$

where τ^{II} is the effective shear stress (second invariant) and $\varepsilon_v^{\text{II}}$ is the effective viscous shear strain (second invariant). The second notion relates to the apparent viscosity determined as

$$\mu_a = \tau^{\text{II}} / \partial(\varepsilon_e + \varepsilon_v + \varepsilon_p)^{\text{II}} / \partial t, \quad (3)$$

where $(\varepsilon_e + \varepsilon_v + \varepsilon_p)^{\text{II}}$ is the total effective shear strain. In computations, we only use the effective viscosity, whereas the apparent viscosity is evaluated for comparison with the results of published viscous models.

Deep mantle convection is weakly dependent on elastic or plastic rheological terms, but this is much less the case for the plume–lithosphere boundary and lithosphere. The Maxwell relaxation time $\tau_m = \mu_{\text{eff}} / E$ in deep mantle is small (100–1000 yr; Appendix B) and the behaviour approaches purely viscous. Yet, just above the plume–lithosphere interface, the relaxation time is 1–10 Myr. In this case, elastic strain becomes as important as viscous strain and the current deformation, plastic or brittle deformation, becomes strongly dependent on strains that have occurred millions of years ago.

3.4 Boundary conditions: the need for a free surface

As shown in studies of gravitational stability of the lithosphere (e.g. Canright & Morris 1993; Molnar & Jones 2004), there can be orders of magnitude differences in the growth rate of perturbations at the lithosphere–asthenosphere boundary, if one compares the case of no slip and that of a stress-free top boundary. There will be even more difference if one considers a free top boundary (no conditions on stress either or displacement). However, there are only a few examples of the application of a free upper surface condition in convection models (e.g. Kiefer & Hager 1992; Solomatov & Moresi 1996). A compromise stress-free upper surface has been implemented in few earlier studies (e.g. Houseman & McKenzie 1982; Craig & McKenzie 1986). A free surface boundary condition, however, makes a major difference in the case of stratified upper layer with EVP rheology, which was not used in these models.

In fixed-top models, surface deformation cannot be computed directly. Instead, it is estimated from the assumption of local isostasy (e.g. Ribe & Christensen 1994). This assumption implies zero lithospheric strength, i.e. no lithospheric flexure or localized deformation. This assumption is also inconsistent with the concept of a stagnant lid implied in these models. The limitations of the fixed upper surface condition are partly circumvented in studies that use a combination of an analytical elastic bending solution for the lithosphere with a viscous flow solution for the plume (e.g. Davies 1992, 1994). However, regional lithospheric deformation involves not only elastic but also inelastic bending (Burov & Diament 1995), necking, faulting, tensional and compressional instabilities (Gerbault *et al.* 1998) that have to be accounted for the realistic prediction of surface deformation.

3.5 Driving forces and plume Rayleigh number

The density contrast between a plume and its surrounding material drives plume ascent and conditions the forces applied at the base of the lithosphere. The density contrast is maximal when the plume arrives at the base of the lithosphere. The thermal part of the density contrast then decays as the plume head material loses heat because of heat diffusion enhanced by plume flattening. To estimate plume-related buoyancy forces, one can consider the density anomaly $\Delta\rho$ resulting from a chemical density difference $\Delta\rho_{\text{ch}}$ and thermal expansion of mantle/plume material (with reference density ρ at T_0) induced by a temperature difference $T = T_0 + \Delta T$ between the plume and surrounding material:

$$\Delta\rho = \Delta\rho_{\text{ch}} + \alpha\rho_m\Delta T, \quad (4)$$

where α is the thermal expansion coefficient and ρ_m is the density of the plume material at the temperature of surrounding material.

Most estimates point to ΔT values on the order of $100^\circ\text{--}300^\circ\text{C}$, which result in $\Delta\rho$ values of $10\text{--}30\text{ kg m}^{-3}$ for no chemical density contrast. These values are approximate because experimental data indicate strong variation of α with temperature and pressure. α first strongly increases (above Moho depths), and then decreases with growing pressure and temperature (Cooper & Simmons 1977; Bauer & Handin 1983). Below the depth at 1300°C ($150\text{--}200\text{ km}$), α starts to continuously decrease with increasing pressure and becomes half as large at $400\text{--}660\text{ km}$ depth. Consequently, if the plume material is buoyant at 410 or 660 km , it may need a higher than conventional ΔT value (up to 500°C) or initial chemical density contrasts (Jaupert, private communication, 2002). Mantle plumes also undergo phase changes and chemical transformations on their way to the surface. It is therefore possible that the chemical density contrast with the surrounding mantle is as important as the thermal contrast. The dependence of the effective viscosity on P–T conditions does not allow one to derive a unique Rayleigh number for the entire system. To circumvent this problem, one can introduce a combination of surface, local and bottom Rayleigh numbers (e.g. Solomatov & Moresi 2000). For our experiments, however, it is useful to operate with a single parameter. For that, we use an effective Rayleigh number for plume ascent (d’Acremont *et al.* 2003). We assume an ascent interval $d - h$ and a maximal driving density contrast $\Delta\rho_{\text{max}}$, where d is the depth to the bottom of the mantle, h is the depth to the bottom of the lithosphere, $\Delta\rho_{\text{max}} = (\rho_p\alpha\Delta T_{\text{max}} + \Delta\rho_{\text{ch}})$ with ρ_p being the density of plume material at the temperature of surrounding material at depth d and ΔT_{max} being the difference between the temperatures of plume material at depths d and h . Assuming representative mean temperature T^* , a simplified approximation for the plume Rayleigh number, Ra_p , reads:

$$\begin{aligned} Ra_p &\approx g\Delta\rho_{\text{max}}(d-h)^3/\chi\mu_{\text{eff}}(r, T^*, \Delta\rho) \\ &= 3^{-(n-1)}Ag^n\Delta\rho_{\text{max}}[r(\Delta\rho_{\text{ch}} + \alpha\rho_m\Delta T)]^{n-1} \\ &\quad \times (d-h)^3/[\chi 6^{n-1}\exp(Q/RT^*)], \end{aligned} \quad (5)$$

where χ is the thermal diffusivity and μ_{eff} is the effective viscosity as defined in eq. (2) and derived in Appendix B.

Instead of Ra_p , a local depth-/temperature-dependent Rayleigh number Ra_b also can be introduced by replacing:

- (i) $d - h$ with a diffusion length scale $\delta = (\pi\chi t_{\text{cr}})^{1/2}$;
- (ii) $\Delta\rho_{\text{max}}$ with $\Delta\rho$;
- (iii) ΔT_{max} with ΔT ; and
- (iv) T^* with T ;

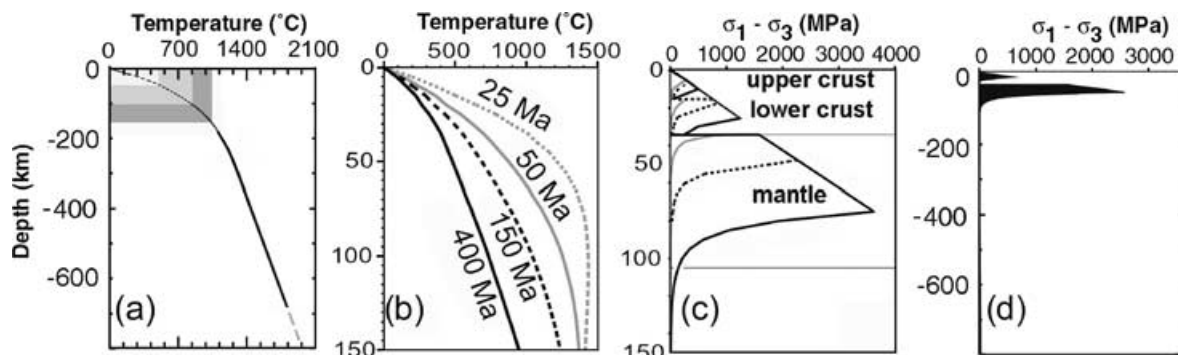


Figure 3. Geothermal profile across the mantle (a) and lithosphere (b), and (c) rheology strength profiles for continental lithosphere as a function of thermotectonic age, assuming a quartz-dominated upper crust and diabase controlled lower crust, for a reference strain rate of 10^{-15} s^{-1} . Frame (d) shows strength profile for 150-Ma geotherm at mantle scale. Ages below 25 Ma, correspond to negligible resistance of the lithosphere. Background temperature at a depth of 650 km is 2000°C .

where t_{cr} can be found from equating Ra_b to critical value Ra_{cr} for the onset of Rayleigh–Taylor (R–T) instability ($Ra_{\text{cr}} \approx 10^3$) or by choosing some other characteristic length scale δ_1 and assuming $t_{\text{cr}} = \delta_1^2/\chi$.

Compared with the case of Newtonian viscosity of the surrounding material, Ra_p for non-Newtonian fluid (e.g. olivine, $n = 3$) reveals strong power-law dependence on the density contrast and on the plume size ($d = 2r$). For Newtonian viscosity, Ra_p is a linear function of the density contrast and does not depend on the plume size. In the case of a non-Newtonian medium, Ra_p scales as a third power of the density contrast (and thus of temperature) and as a second power of the plume size. Plume ascent through a non-Newtonian fluid is thus extremely sensitive to effective body forces. A very small variation in buoyancy force results in a strong variation in the ascent behaviour. For an equivalent body force, this ascent may be orders of magnitude faster than for a Newtonian fluid (Weinberg & Podladchikov 1994).

3.6 Sublithosphere geotherm

Computation of buoyancy forces needs to account for the mantle geotherm (Fig. 3). The real thermal structure of the upper mantle is poorly known and, for this reason, a near adiabatic geotherm associated with the notion of potential temperature is often used to compute buoyancy forces (Schubert *et al.* 2001). This assumption becomes self-contradictory in the case of high Rayleigh numbers. As long as the assumed plume temperature and/or density contrast is significant, the peculiarities of the background geotherm are not important if the numerical code is fully thermally coupled. In the numerical code PAROVOZ used for this study, the temperature field from the previous time step is used for the computation of driving forces on the current time step. This approach is suitable for plume ascent because the driving forces depend on the local temperature field perturbed by the plume as much as on the regional field.

4 NUMERICAL SETUP

In order to focus our study on plume head—continental lithosphere interactions, we use a numerical method that accounts for a realistic rheology and upper surface conditions. This code (PAROVOZ, Poliakov *et al.* 1993) has been derived from the FLAC algorithm (Cundall 1989). Its rift and plume version is explained in detail in Burov & Poliakov (2001) and d’Acremont *et al.* (2003), and is briefly described in Appendices A and B. To account for all

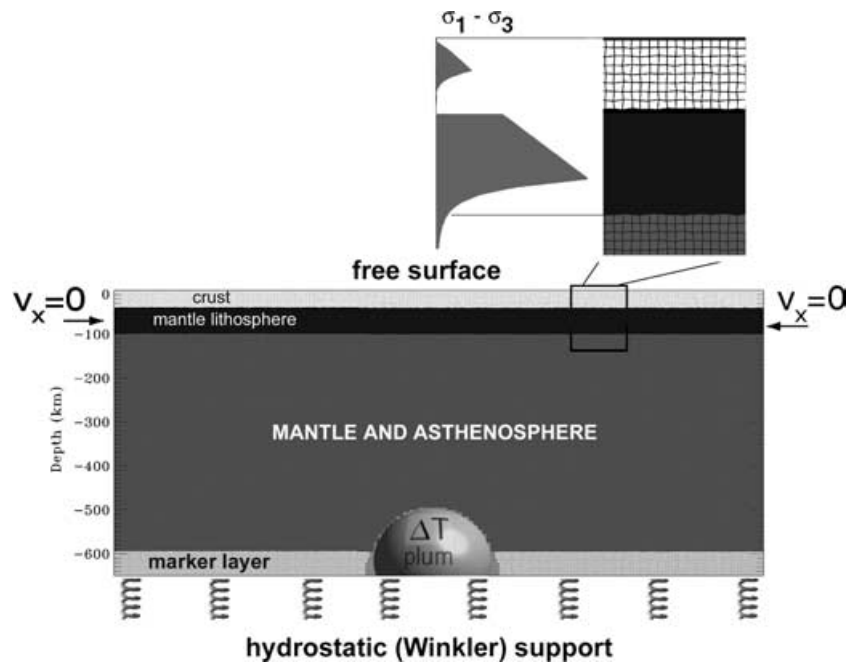


Figure 4. Experiment setup and boundary conditions. The initial plume size varies from 100 to 200 km. The lithospheric thickness varies from 100 to 200 km. The lateral box size varies from 1000 to 2000 km. V_x is horizontal velocity. Zoomed box shows strength profile and initial grid geometry in the lithospheric domain. Initial grid angles are artificially perturbed using 0.2 per cent white noise to simulate a natural heterogeneous structure of the mantle and lithosphere.

possible types of deformation (including pressure- and strain-dependent lithospheric deformation), this method solves Newtonian equations of motion (second law) directly instead of the Navier–Stokes equations. The algorithm explicitly takes into account physical elastic–brittle–ductile properties of the mantle, crust and lithosphere, and handles brittle and ductile strain localization, allowing us to model the formation of brittle faults and ductile shear zones. The algorithm includes an explicit free upper surface boundary condition.

4.1 Model geometries

The plume–continental lithosphere interactions are restricted to the upper mantle (650 km depth). For this reason, the vertical size of the model is also limited to 650 km. The horizontal size of the box varied between 1000 and 2000 km (Fig. 4).

Following Ribe & Christensen (1994), we do not consider the initial stages of diapir formation, as they are of minor importance for near-plate processes. The initial mantle plume (spherical density contrast) is located at the base of the model box and has a diameter of 100–200 km. Because the plume head is deformable, the choice of initial geometry is of minor importance. The choice of spherical geometry is supported by fact that a viscous body takes a spherical shape in a laminar regime and infinite space (Batchelor 1967). In the middle-mantle conditions, the diapiric ascent occurs at Reynolds numbers well below 10^5 and thus in the laminar regime.

Several lithospheric structures have been tested in order to encompass end-member situations, including the probable case of a hot, thin Archean continental lithosphere. In the first set of experiments (Fig. 4a), the lithosphere was young (150 Ma) and thin (100 km). In the second set (Fig. 4b), the thermal structure and rheological structure of the lithosphere corresponded to an old (400 Ma) and thick (200 km) continental lithosphere. The 400-Ma age corresponded to characteristic decay time within which continental geotherms ap-

proach steady state (Parsons & Sclater 1977). The age dependence of the lithospheric geotherm is still non-negligible until 800–1 Ga (e.g. Perry & Jaupart 2004), but major cooling occurs within the first 400 Myr.

4.2 Density and rheological structures

Each numerical element is assigned its specific material phase, which is defined as a set of physical parameters of given material: density, thermal and rheological (elastic, ductile and brittle) parameters (Tables 1 and 2). We use a conventional density structure for the mantle, including the lithosphere (Turcotte & Schubert 2002). All continental models include 40-km-thick crust and four horizontal rheological layers (Tables 1 and 2; Carter & Tsenn 1987; Kirby & Kronenberg 1987):

- (i) a 20-km-thick granite upper crust with a density of 2700 kg m^{-3} ;
- (ii) a 20-km-thick granite lower crust with a density of 2900 kg m^{-3} ;
- (iii) 60- or 160-km-thick olivine lithosphere with a density of 3330 kg m^{-3} ; and
- (iv) deeper mantle with a reference mantle density of $\rho_m = 3400 \text{ kg m}^{-3}$ at 200 km (Turcotte & Schubert 2002).

The density of the plume has the same dependence on pressure as the background ($\rho_p = \rho_m + \Delta\rho_{ch} + \alpha\rho_m\Delta T$). For this reason, the absolute values of background density are of no importance. A uniform numerical grid provides vertical and horizontal resolution of $5 \text{ km element}^{-1}$. The lithospheric layer thus includes 30 to 50 elements in the vertical direction, which corresponds to 10–15 times higher resolution than in most previous models (e.g. Ribe & Christensen 1994).

The rheology chosen for crust and mantle is an EVP rheology with a quartz(granite)-dominated crust and an olivine-dominated

Table 1. Notations and physical values common for all experiments (Schubert *et al.* 2001; Turcotte & Schubert 2002).

Parameter	Values and units	Definition
σ, τ	Pa, MPa	Stress
P	Pa, MPa	Pressure
v	m s^{-1} , mm yr^{-1}	Velocity vector
μ	10^{19} – 10^{25} Pa s	Effective viscosity
$\dot{\epsilon}$	s^{-1}	Strain rate
T	$^{\circ}\text{C}$	Temperature
h_c	7 km/40 km	Moho depth (oceans/continents)
h_l	100–200 km	Thickness of lithosphere
D	100–200 km	Plume diameter
ρ_l	3330 kg m^{-3}	Density of mantle lithosphere
ρ_m	3400 kg m^{-3}	Reference deep mantle density (at 200 km depth)
ρ_p	$\rho_m + \Delta\rho_{\text{ch}} + \alpha \rho_m \Delta T$	Plume density
$\Delta\rho_{\text{ch}}$	0–25 kg m^{-3}	Chemical density contrast
g	9, 8 m s^{-2}	Acceleration as a result of gravity
C_p	$10^3 \text{ J Kg}^{-1} \text{ }^{\circ}\text{C}^{-1}$	Specific heat
ΔT	250°C	Initial temperature contrast plume—background
α	$3 \times 10^{-5} \text{ }^{\circ}\text{C}^{-1}$	Thermal expansion

Table 2. Specific rheology and related thermal parameters. Compilation by Burov & Poliakov (2001). ρ is density; Q , n , A are material-dependent parameters of ductile flow laws (Kirby & Kronenberg 1987; Kohlstedt *et al.* 1995). Other parameters from Turcotte & Schubert (2002).

Parameter	Value
<i>All rocks</i>	
λ, G Lamé elastic constants ($\lambda = G$)	30 GPa
ϕ friction angle (Mohr–Coulomb rheology)	30°
C_0 cohesion (Mohr–Coulomb rheology)	20 MPa
<i>Specific upper-crust and weak (quartz) lower-crust properties</i>	
ρ (upper crust)	2700 kg m^{-3}
ρ (lower crust)	2900 kg m^{-3}
n (power-law exponent)	2.4
A (power-law constant)	$6.7 \times 10^{-6} \text{ MPa}^{-n} \text{ s}^{-1}$
Q (creep activation enthalpy)	$1.56 \times 10^5 \text{ kJ mol}^{-1}$
<i>Specific strong lower crust properties (diabase or basalt)</i>	
ρ	2980 kg m^{-3}
n (power-law exponent)	3.4
A (power-law constant)	$2 \times 10^{-4} \text{ MPa}^{-n} \text{ s}^{-1}$
Q (creep activation enthalpy)	$2.6 \times 10^5 \text{ kJ mol}^{-1}$
<i>Specific mantle properties (olivine)</i>	
ρ (lithosphere)	3330 kg m^{-3}
n (power-law exponent)	3
A (power-law constant)	$1 \times 10^4 \text{ MPa}^{-n} \text{ s}^{-1}$
Q (creep activation enthalpy)	$5.2 \times 10^5 \text{ kJ mol}^{-1}$
<i>Thermal model</i>	
Surface temperature (0 km depth)	0°C
Temperature at the bottom of thermal lithosphere	1330°C
Temperature at 660 km depth	2000°C
Thermal conductivity of crust k	$2.5 \text{ W m}^{-1} \text{ }^{\circ}\text{C}^{-1}$
Thermal conductivity of mantle k	$3.5 \text{ W m}^{-1} \text{ }^{\circ}\text{C}^{-1}$
Thermal diffusivity of mantle χ	$10^{-6} \text{ m}^2 \text{ s}^{-1}$
Radiogenic heat production at surface H_s	$9.5 \times 10^{-10} \text{ W kg}^{-1}$
Radiogenic heat production decay depth h_r	10 km
Thermotectonic age of the lithosphere a	150 Myr (young) and 400 Myr (old)

mantle (Table 2; Ranalli 1995; Burov & Cloetingh 1997). The elastic and brittle parameters are provided in Table 2 and are explained in Appendix B.

4.3 Boundary and initial conditions

The initial background geotherm is obtained by joining continental and deep mantle geotherms. The initial age-dependent cooling

geotherms for the lithosphere are computed according to Parsons & Sclater (1977) and Burov & Diament (1995). At the depth at 1330° (thermal base of the lithosphere), these geotherms transform themselves into adiabatic geotherms (approximately 0.3 – $0.5^{\circ}\text{C km}^{-1}$; Schubert *et al.* 2001; Sleep 2002). Temperature slowly increases from 1330° to 1450°C at 400 km depth and reaches 2000°C at 650 km depth (e.g. Schubert *et al.* 2001). As discussed above,

peculiarities of geotherms in the mantle domain are of little importance because (i) the density contrasts associated with the diapir are more important than density variations of the background field, and (ii) the temperature field is recomputed on each time step and the buoyancy forces are re-adjusted according to the actual (and not the initial reference) thermal distribution.

Zero heat flux is assumed as a lateral thermal condition on both sides of the box. The surface temperature is fixed at 0° C and the bottom temperature is fixed at 2000° C.

The mechanical boundary conditions assigned on the four sides of the box (Fig. 4) are: on the left and right sides, horizontal velocity is $v_x = 0$; hydrostatic pressure is applied at the bottom; a free surface is imposed as the upper boundary condition.

5 RESULTS

Most of the results described below are discussed in terms of the predicted surface topography. Consequently, we first show differences between tests with Newtonian and non-Newtonian rheology, when a plume impinges at the base of an oceanic lithosphere (d'Acremont *et al.* 2003). The description of this reference calculation is followed by an investigation of additional effects.

5.1 Reference calculations and benchmarking (oceanic lithosphere)

The code has been previously tested in Burov *et al.* (2001) against the analytical solution for the non-Newtonian Stokes problem (Weinberg & Podladchikov 1994; Appendix B). For mantle scale reference calculations, we have also run several benchmark experiments (see also d'Acremont *et al.* 2003) assuming a common setup that includes a homogeneous (oceanic) lithosphere with Newtonian rheology and a fixed upper surface. These experiments were then compared with experiments on homogeneous lithosphere with non-Newtonian rheology and a free surface (Fig. 5). The initial temperature anomaly ΔT and the equivalent density contrast between the plume and the asthenospheric mantle were respectively 300° C and 30 kg m⁻³ (Farnetani & Richards 1994; Ribe & Christensen 1994). We varied these parameters in a wide range of possible values from 100° to 300° C, and from 10 to 25 kg m⁻³, respectively (d'Acremont *et al.* 2003). Fig. 5 demonstrates differences in the topographic signatures associated with the impingement of a plume head beneath an oceanic lithosphere, where a conventional New-

tonian model with a rigid top is compared with a non-Newtonian model with a free upper surface. In the case of a free surface and non-Newtonian EVP rheology, the amplitude of vertical uplift is 30 per cent smaller than for the isostatic Newtonian prediction, which matches estimates by (Ribe & Christensen 1994) for similar conditions (Figs 5a and b). Moreover, the shape of the surface doming is also quite different: secondary short-wavelength harmonics are observed in the non-Newtonian reference model (Fig. 5, case c) as a result of localized plate weakening.

Fig. 6 shows a reference experiment with an oceanic-like thin lithospheric monolayer, analogous to those of d'Acremont *et al.* (2003). In this and following figures, time increases from bottom to top and physical parameters are shown: rheological phases, velocity field, temperature field and effective viscosity. Strain rates are also computed and shown when required. Time steps were chosen to emphasize specific plume behaviour or evolution of topography and thus can be different from one test to another. In Fig. 6, the plume head arrives at the bottom of the lithosphere and flattens over a large regional scale. At the first stage, a small-scale domal uplift develops superimposed on large-scale domal uplift (see right column in Fig. 6, wavelength of 300 km). Upon its arrival, the plume head erodes and destabilizes the colder, heavier lithosphere, which develops an R–T-like instability and sags down. As a result, the plume head is divided into two diverging zones resulting in the formation of alternating zones of extension and compression in the overlying lithosphere, and hence in two series of zones of uplift and subsidence (time step of 5 Myr). In contrast with the previous studies (e.g. Sleep 2003), lithospheric downwellings are not only conditioned by the density, temperature and viscosity of the uppermost mantle, but also by mechanical properties, density and temperature of the crust, which is unlikely to sink as a result of its large positive buoyancy (Table 1).

5.2 Thin (hot) continental lithosphere

In this set of experiments, the initial lithosphere is hot and thin (100 km; Figs 7 and 8). For this case, we tested two main situations:

(i) a laterally homogeneous lithosphere with an initial geotherm corresponding to 150 Myr included in a system with a relatively low plume Rayleigh number (10^5 , background subasthenospheric viscosity cut-off, or mean background viscosity, $\mu \geq 10^{20}$ Pa s); and

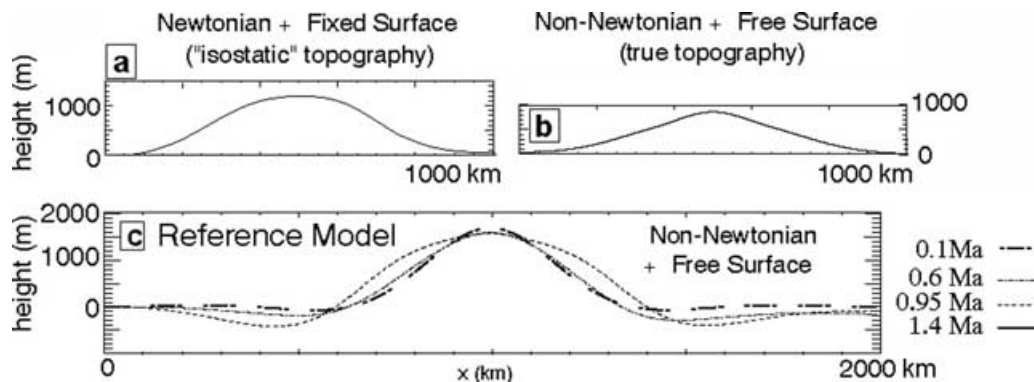


Figure 5. Reference calculations. Comparison of topographic signatures of plume–oceanic lithosphere interaction. Oceanic case includes thin 100-km-thick, 1000-km-long lithosphere with no crust (see Tables 1 and 2). Results of test models at $t = 1.4$ Ma. (a) Conventional setup for a benchmark test with Newtonian rheology and a fixed-surface boundary condition. Effective topography for the benchmark test is computed assuming local isostasy ($\Delta T = 300^\circ$ C, $\mu = 10^{20}$ Pa s). (b) Free surface and non-Newtonian EVP rheology. $Ra_p = 2.7 \times 10^5$ ($\Delta T = 300^\circ$ C, effective viscosity at depth $\mu \geq 10^{20}$ Pa s). (c) Reference model $Ra_p = 2.66 \times 10^5$ ($\Delta T = 300^\circ$ C, $\Delta\rho = 30$ kg m⁻³, viscosity $\mu \geq 10^{20}$ Pa s, horizontal scale 2000 km). In cases of EVP rheology, the effective viscosity varies from 10^{25} Pa s at top to 10^{20} Pa s at bottom of the plate.

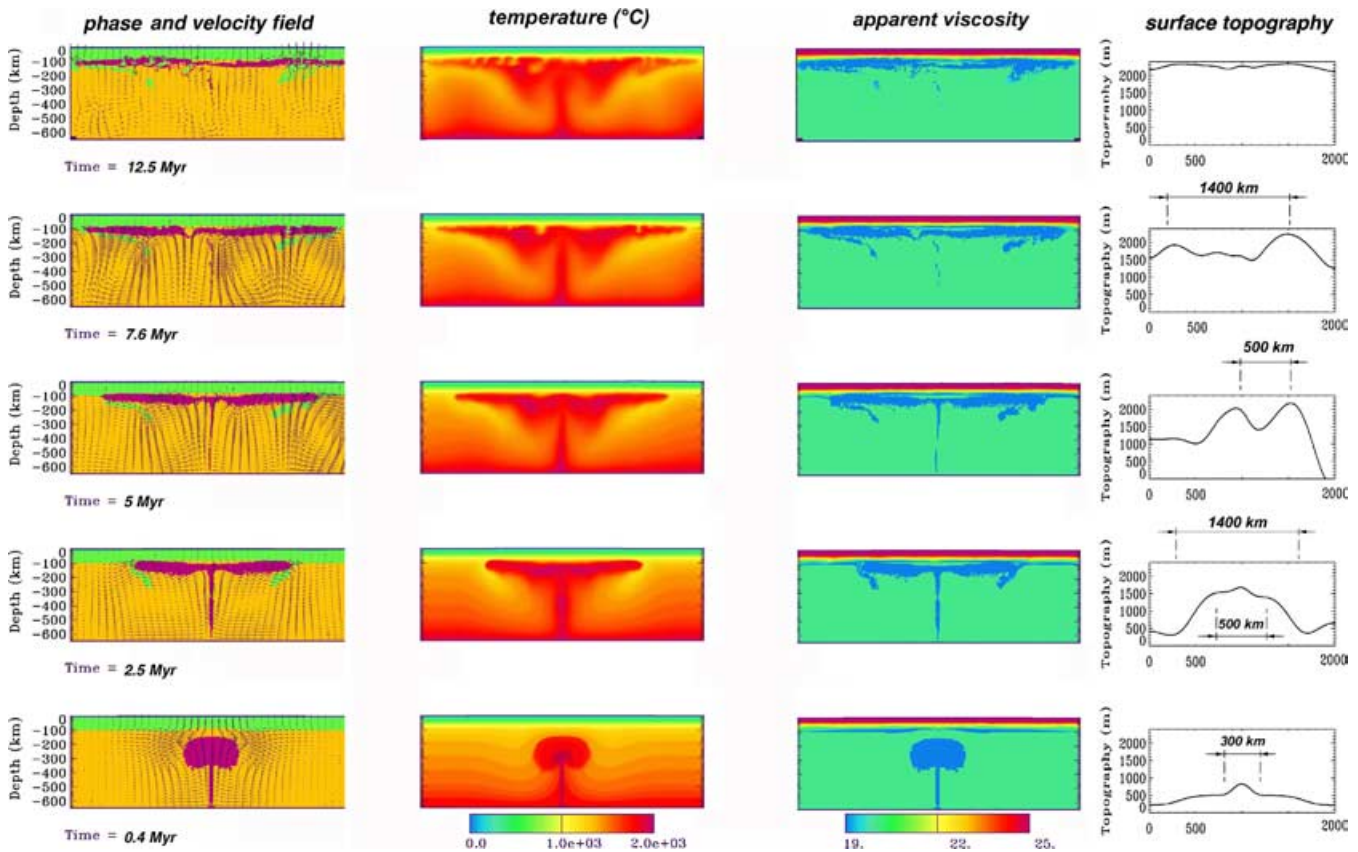


Figure 6. Experiments with thin monolayer oceanic-type lithosphere, EVP rheology ($Ra_p = 10^5$; $\Delta T = 250^\circ \text{C}$; background viscosity at depth $\mu \geq 10^{20} \text{Pa s}$). Shown from left to right are: phase and velocity fields; temperature field ($^\circ \text{C}$); apparent viscosity (Pa s); elevations (m). Colour code (see pdf/html version of the paper) for the phase field is: blue, oceanic crust (7 km thick); green, olivine lithosphere; yellow, olivine/peridotite mantle; purple, plume material. Each phase corresponds to a set of rheological and physical parameters describing distinct material (rheological parameters, thermal properties, density). The apparent viscosity is computed for viscous, elastic and ductile domains as a ratio of instantaneous stress and strain rate.

(ii) the same experiment with a higher plume Rayleigh number (10^6 , background subasthenospheric viscosity cut-off $\mu \geq 10^{19} \text{Pa s}$).

Figs 7 and 8 repeat the experiments of Fig. 6 assuming a thin 150-Myr-old, multilayer continental lithosphere. Figs 7(a), 8(a) and (b) show the cases of $Ra_p = 10^5$, $Ra_p = 10^6$ and $Ra_p = 5 \times 10^6$, respectively. In these experiments, light, weak (quartz rheology) crust that initially keeps heavier mantle lithosphere afloat can be mechanically decoupled from it, as a consequence of both thermal and strain rate softening produced by interaction with the plume head. As a result, the plume head can destabilize the mantle part of the lithosphere (see distribution of rheological phases, left column in Figs 7a and 8a), which starts sinking down quasi-immediately after crust–mantle decoupling. It follows that a large zone of mantle lithosphere above the plume head develops R–T-like and intraplate tensional instabilities. Thus, instead of a single domal uplift, a series of large-scale uplifts and basins are formed in the surface as a result of mechanical decoupling of the crust and the mantle (see surface topography signatures, right columns in Figs 7b and c). Comparison with the monolayer case suggests that the layered structure of continental lithosphere plays a first-order role in the surface reaction to plume ascent. In general, decoupling results in the appearance of two or three harmonics of surface deformation. This effect of crustal–mantle decoupling was discussed in a number of studies on lithospheric deformation (e.g. Gerbault *et al.* 1998) but was not related to plume–mantle interactions. The main differences between Figs 7(a), 8(a) and (b) are

clearly expressed in the predicted topographic signatures. The low Ra_p case shows a large-scale depression, as a result of a large-scale plume-induced basal drag, compared with higher Rayleigh number cases, in which plume impacting becomes significant, and induces uplift and subsidence signatures. Yet, wavelengths of these surface undulations are not only controlled by Ra_p , as it is explained below. Also noteworthy are secondary-scale plumes initiated at the bottom of the box a few Myr after the ascent of the initial plume (Figs 8a and b). These secondary plumes may be responsible for secondary phases of extension. However, their formation depends on the assumed thermal condition on the bottom (fixed temperature). In the case of a fixed flux boundary condition, the initiation of secondary plumes may be less favoured.

5.2.1 Plume ascent and plume head flattening

Plume head flattening begins when its upper extremity approaches the bottom of the lithosphere. Peculiar features of this process can be observed in the velocity, temperature, effective viscosity and phase fields (Figs 7a, 8a and b). The velocity field shows two distinct convective cells, and the material phase field shows lobes situated on either side of the plume head and present only in the asthenospheric mantle. These lobes propagate horizontally at a rate comparable to the plume ascent rate. The strain rate field indicates two areas of strain localization at the bottom of the lithosphere above the plume head (Fig. 7b). As it flattens, the plume head is separated into several

zones as a result of R–T instabilities and boudinage of the uppermost lithosphere (Fig. 7c). This mechanism explains the formation of alternating series of basins and uplifts with a wavelength of 300–400 km, as shown in the early stages of Figs 8(a) and (b) and partly visible at the latest stage of Fig. 7a.

5.2.2 Thermomechanical erosion

A significant thickness of the lithospheric mantle is eroded and reworked by the plume. As the plume head flattens, the lithosphere is mostly eroded in two large areas adjacent to the centre of the plume head, where the strain rates are maximum (Fig. 7b). This favours the formation of alternating zones of lithospheric extension (downs) and compression (ups). The deformation increases under the lithosphere while strain rates in these two areas become large. The border zones of the eroded area are characterized by pronounced downwelling of cold lithospheric material, all the more when Ra_p is low. The erosion occurs initially because of strain-rate weakening, not because of thermal softening, which needs more time because of locally high Peclet numbers. Shear stresses created in the lithosphere by interaction with the plume head result in stress localization on the order of $\pm 1\text{--}110$ MPa within the first 50–100 km of the lithosphere, which remains effectively elastoplastic (brittle) and non-viscous. High shear strains are also localized above the rising plume and over both edges of the plume head (Fig. 7b). The plume head, which had an initial diameter of 200 km, becomes 1000 km wide under the lithosphere (Figs 7a, 8a and b). In some cases, the mantle part of the

lithosphere is thinned and weakened above the plume head to the extent that it decouples from the underlying buoyant crust and becomes gravitationally unstable. As a consequence, R–T instabilities develop and the lithosphere sags into the plume head. This is more important for relatively low Ra_p (Figs 7c and 8a). With an increasing Rayleigh number, large-scale lithospheric erosion vanishes as a result of decreased shear stresses and the reduction of the thickness of the critical thermal layer below the interface plume–lithosphere. The wavelength of bottom instabilities is thus reduced, resulting in the formation of a laterally spreading zone of small-scale erosion, and vigorous local downwellings penetrate through the ponded plume material (Fig. 8b), as a number of studies have shown (e.g. Sleep 2003).

5.2.3 Extensional events

The experiments predict two main phases of extensional evolution. First, large-scale extension over the centre of the plume head occurs at early stages of plume ascent and follows initial domal uplift after approximately 0.5 Myr since initiation of the plume at depth. This extensional event is then likely to be followed by second phase of extension resulting in the formation of a system of alternating basins (one or no central basin and two basins aside) spaced at 300–400 km (Figs 8a and b). The initial central basin is often subject to boudinage resulting in the formation of small-scale basins (and ranges) with a spacing of 100–200 km inside the central basin.

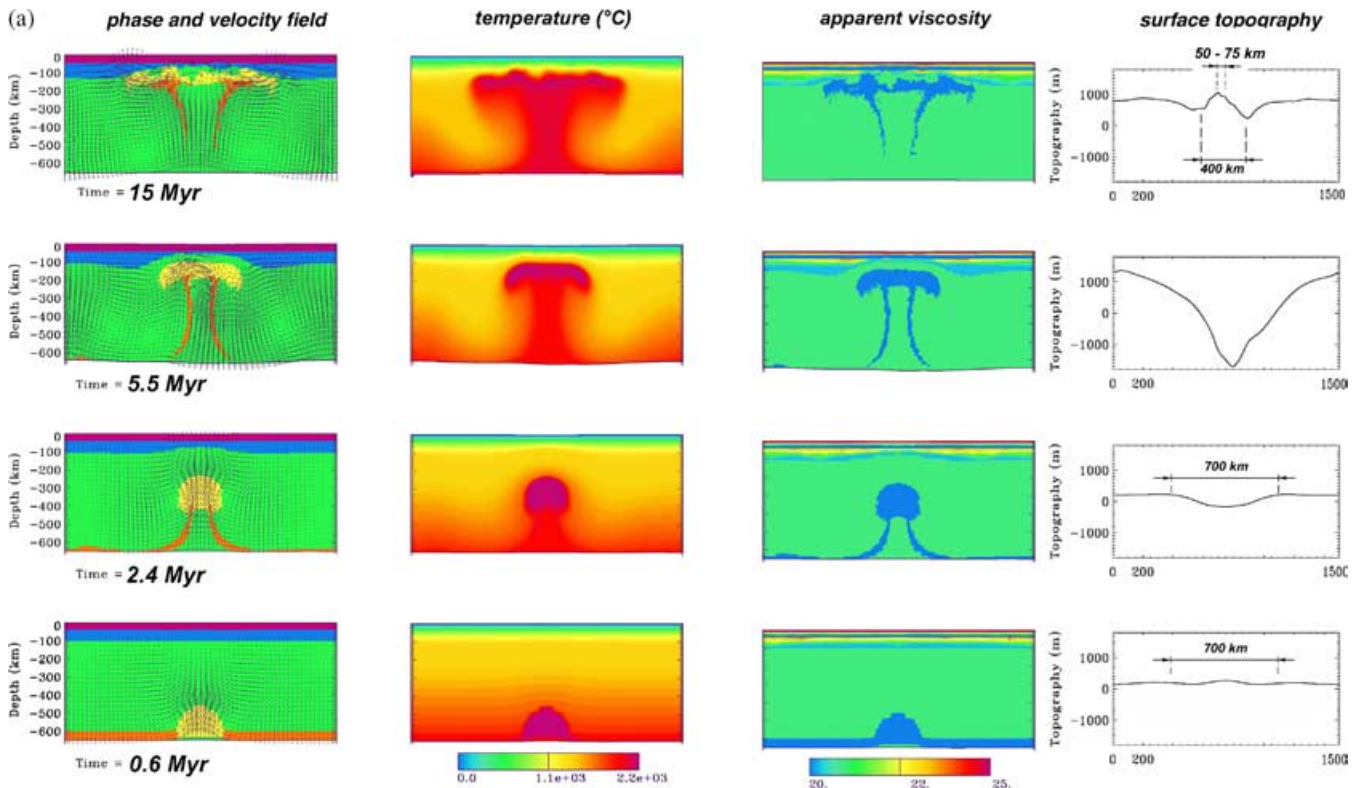


Figure 7. Experiments with a thin three-layer laterally homogeneous continental lithosphere. The initial thermotectonic age is 150 Ma, $Ra_p=10^5$ and background viscosity at depth $\mu \geq 10^{20}$ Pa s. Note the multiharmonic character of surface deformation resulting from the interaction between different rheological layers within the lithosphere. For more detail, see colour pdf/html version of the paper. (a) Main stages of evolution. Shown from left to right are: the phase field; temperature field ($^{\circ}$ C); topography elevations (m). Colour code for the phase field in the pdf/html version of the paper is: purple, continental crust (40 km thick); blue, olivine lithosphere; green, olivine/peridotite mantle; yellow and orange, plume material. (b) Zoom of snapshots of the lithosphere showing the strain rate field (\log_{10}) at 5.5 and 15 Myr. (c) Zoom of snapshots of the lithosphere showing the apparent viscosity field in the lithosphere at 15 Myr. Note periodic variations of apparent viscosity related to extensional instabilities, and the development of basins and ranges.

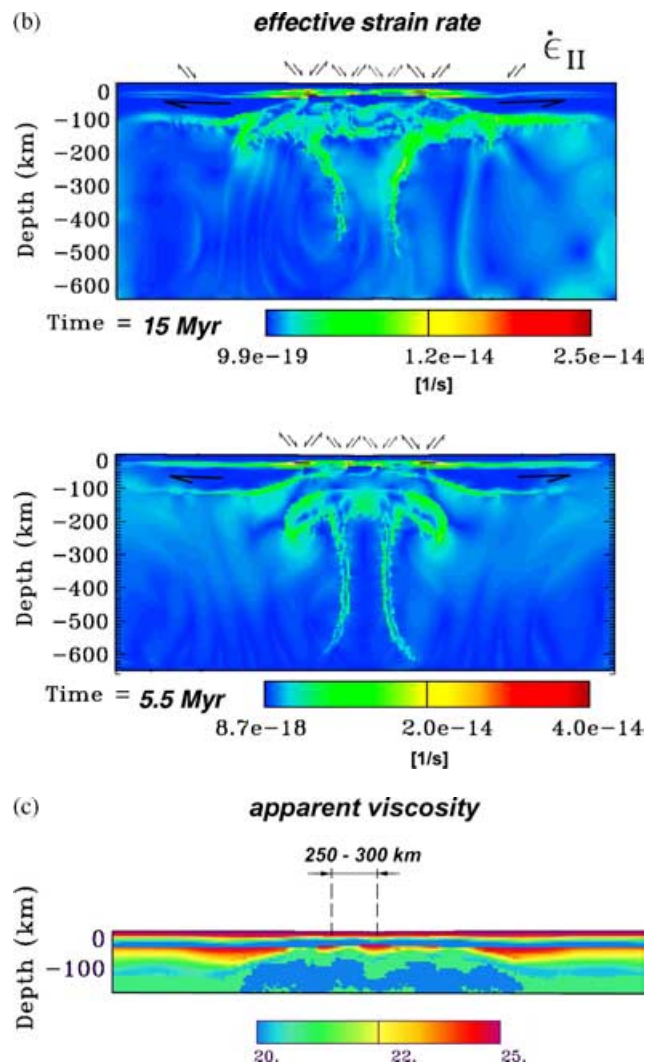


Figure 7. (Continued.)

5.2.4 Predicted surface uplift

Not only the wavelength but also amplitudes of surface uplift are conditioned by layered rheology and a free surface boundary condition. In general, the amplitudes of the surface uplift are 2–30 per cent smaller than those that could be predicted based on isostatic assumptions (Fig. 5). The wavelength is controlled not only by plume head flattening but also by the thickness of the competent crust and mantle. Large-scale uplift associated with plume flattening is superimposed on two smaller wavelengths corresponding to decoupled deformation of the mantle and crustal layers. According to theory of boudinage (Smith 1975), these wavelengths are proportional to 5–10 thicknesses of the corresponding competent layer. Crustal wavelength is thus limited to approximately 50–200 km but the mantle wavelength may vary from 50 to 1000 km (depending on the geotherm and rheology). In the case of 150-Myr lithosphere, the mantle wavelength is close to the crustal wavelength (200–300 km) resulting in interference between crustal and mantle deformation. The amplitudes of surface uplift are quite sensitive to a number of parameters. Previous numerical results (Monneréau *et al.* 1993) predict a two-phase surface uplift, e.g. the first phase produces approximately 700 m uplift at the centre of the plume and the second phase results in a maximum uplift of 1300 m after 40 Ma. Semi-

analytical estimations by Davies (1994) predict an initial uplift of 500 m and a consequent 1500 m uplift, resulting from erosion of the lithosphere. Experiments based on the local isostatic assumption (Ribe & Christensen 1994; Manglik & Christensen 1997; Cserepes *et al.* 2000) find a maximum topographic uplift of approximately 1300–1350 m.

In the case of 150-Ma layered lithosphere, our model predicts a long-wavelength dynamic surface uplift with an amplitude of <800 m achieved after the first 0.4 Myr (Fig. 7,8). At this moment, the plume head is still very deep (at 300–350 km depth). The major long-wavelength elevation event (1000 m) occurs at 1–2.5 Ma. The highest elevations recorded during experiments are on the order of 1000 m at 2.5 Myr after the onset of plume ascent. During the following evolution, middle-wavelength (<300 km) elevations of 700–800 m are progressively superimposed on the regional uplift field. As can be seen, the amplitudes of surface elevations in the case of layered lithosphere are approximately half of those recorded for single-layer oceanic lithosphere.

Simulations that compare the effect of different background viscosities show that the velocity of the rising plume and the strain rate field are strongly dependent on the viscosity contrast (i.e. viscosity gradient) at the transition between the lithosphere and underlying mantle (Figs 7 and 8). When the asthenospheric mantle viscosity is reduced by 1 order of magnitude (from 10^{20} to 10^{19} Pa s), the basal lithospheric erosion becomes stronger, just as the lithospheric thinning also becomes more important and considerably faster. It thus appears that the strain rate is highly dependent on the viscosity profile through the lithosphere–asthenosphere transition as well as on the plume–asthenosphere viscosity contrast. The vertical thinning rate appears to be only weakly dependent on the lateral scale of the upwelling, contrary to the geometry and evolution of the area of horizontal thinning, which is dependent on the length of the plume head flattening.

5.2.5 Predicted lithospheric stress and strain distributions

Stress and strain patterns in the lithosphere (Fig. 7b) demonstrate alternating zones of extension (basins, normal faulting) and compression (ranges, uprisings, inverse faulting). Because the brittle strength is 1.5 times higher in compression than in tension (see Appendix A), reverse faulting is far less frequent than normal faulting. The shear and normal deviatoric stress fields predict stress localizations on the order of ± 85 –120 MPa within the first 70 km depth interval that remains effectively elastoplastic and non-viscous. The horizontal extensional stress is localized within the elastoplastic part of the crust and mantle lithosphere above the rising plume. The ascent of the plume results in upward lithospheric flexure, which, in turn, causes additional extension and irreversible plastic failure (faulting). Compressional lithospheric stresses are observed over both edges of the plume head. There is a moderate propagation of convective cells right into the lithosphere, but it does not affect more than half of the initial lithospheric thickness (see velocity fields in Figs 7a and 8a).

The shear stress field indicates extensional stresses above the rising plume and compressional stresses on the edges, within the first 70–100 km depth.

5.3 Thick (cold) continental lithosphere

Fig. 9 demonstrates results for initially old and cold lithosphere (400 Ma). In this case, three main phenomena are observed:

- (i) the increase of the lithospheric thickness reduces the Rayleigh number of the convective system, and results in slower and less active background motion;
- (ii) the lithosphere has a more important integrated strength, which results in long-wavelength, small amplitude deformation at surface; and
- (iii) in some cases, crust–mantle coupling occurs, which almost doubles the integrated flexural strength of the lithospheric plate (Burov & Diament 1995) with obvious consequences for surface evolution, such as only large-scale doming without formation of alternating basins.

These conditions would correspond to the case of the coldest and thickest continental lithosphere, which may be found in Archean terrains.

5.4 Influence of plume geometry

Fig. 10 demonstrates the influence of the plume size on the lithospheric and surface evolution. For a plume head size ($D = 100$ km) half that in the previous experiments, the surface deformation occurs at slightly smaller wavelength (400 km) and large-scale deformation is superimposed, at some initial stages, with 50–75 km wavelength

deformation corresponding to crustal instabilities. The wavelength of these instabilities is proportional to 5–10 thicknesses of the competent layer. A smaller plume head results in concentrated flexural deformation of the uppermost lithosphere that yields locally higher bending stresses. These stresses favour decoupling of a thin brittle crustal layer of only 10–15 km that deforms in an unstable regime separately from the rest of the lithosphere (e.g. Burov & Diament 1995). Small-scale crustal deformation is also observed in a number of previous experiments with a large plume head, for example for high Ra_p associated with typical small-scale mantle instabilities (e.g. Sleep 2003), or in zones of concentrated crustal thinning (= reduction of thickness of competent layers). The other possible reason for the appearance of small-scale crustal deformation may be related to the plume tail size, which increases with time. In our experiments (Figs 6, 7, 8, 9 and 10), plume head flattening is often preceded by tail widening, and it appears that tail sizes and wavelengths of topographic signatures are surprisingly correlated. Furthermore, when the tail size increases with time, small wavelengths disappear. Although the bulk plume geometry is partly defined by rheological contrasts (Schubert *et al.* 2001), plume head sizes and plume tail sizes are not necessarily related, and dynamic features of each may play a role in the resulting surface deformation. This test suggests

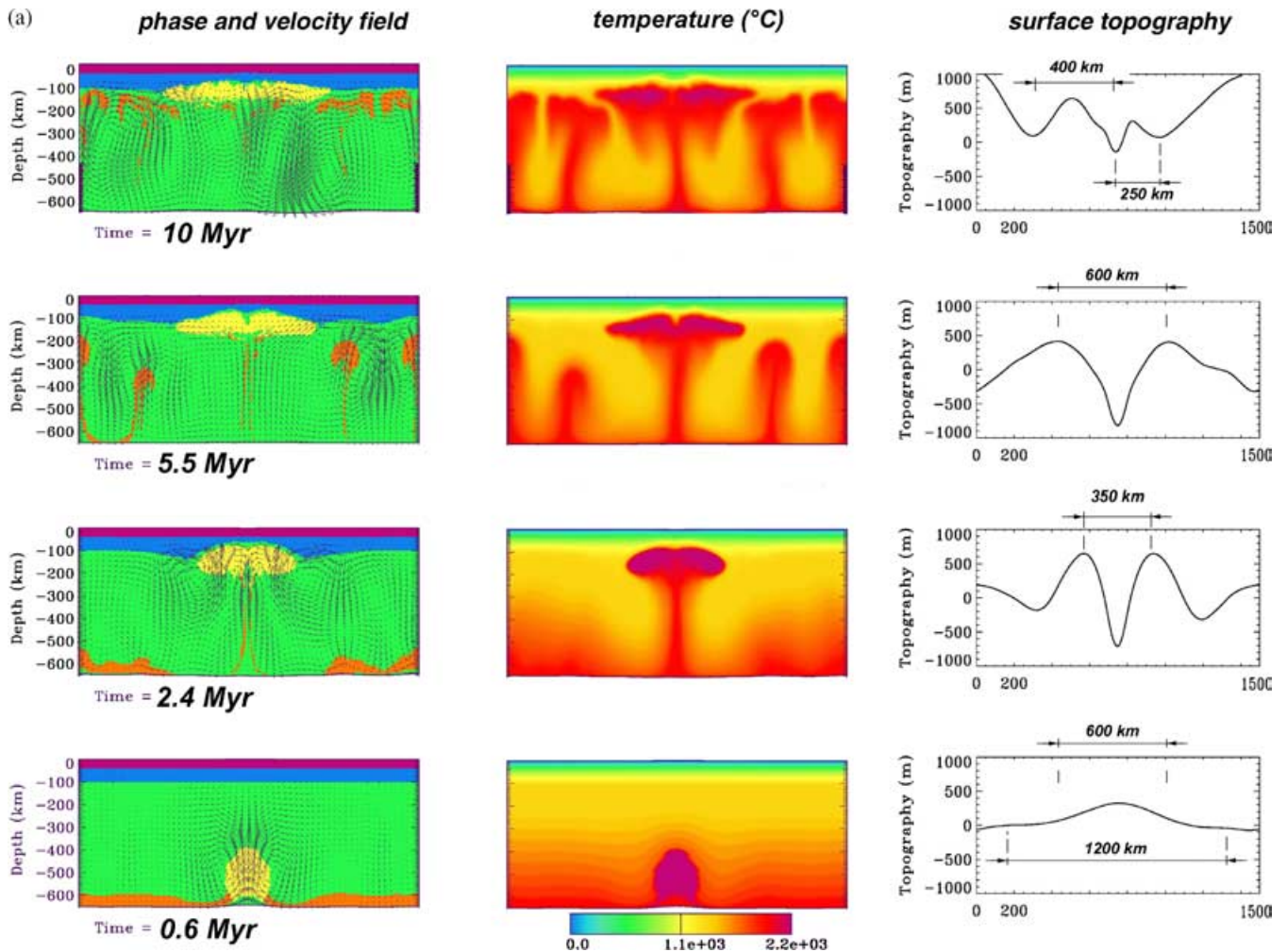


Figure 8. Experiments with a thin three-layer laterally homogeneous continental lithosphere analogous to those of Fig. 7 but for higher Ra_p numbers. (a) $Ra_p = 10^6$; background viscosity at depth $\mu \geq 5 \times 10^{19}$ Pa s. (b) $Ra_p = 5 \times 10^6$; background viscosity at depth $\mu \geq 10^{19}$ Pa s. The wavelength of bottom instabilities in case (b) is reduced resulting in the formation of a laterally spreading zone of small-scale erosion and vigorous local downwellings that penetrate through the ponded plume material. For more detail, see colour pdf/html version of the paper.

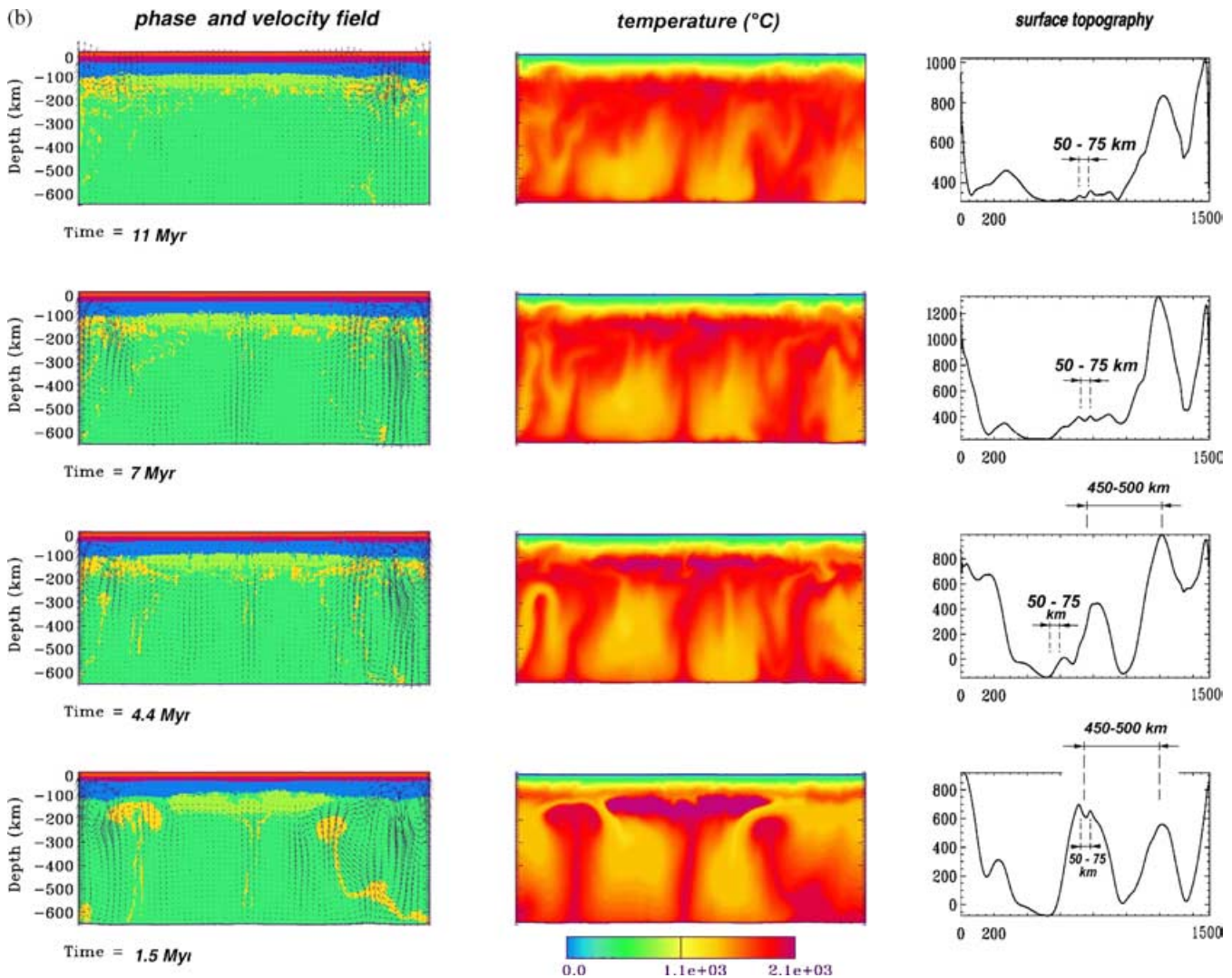


Figure 8. (Continued).

that surface signatures are not only a function of lithospheric rheology (and thus of lithospheric age and thickness), but also depend on plume dynamics, which are themselves driven by deeper processes. A complete study of plume geometry effects on lithospheric deformation would require additional tests that are beyond the scope of this study.

6 IMPLICATIONS FOR TOPOGRAPHY ASSOCIATED WITH A MANTLE PLUME

The above described series of extensional events, together with spatial and temporal variations of uplift and subsidence phases, can be compared with geological observations of rifting-related surface signatures. Numerous field observations allow us to suggest that the conventional model of plume-induced uplift, basically a single-wavelength signature, does not apply to continental lithosphere. When a mantle plume is inferred from geochemical and geophysical data over a continental area, the topographic and volcanic signatures may not be as evident as beneath an oceanic lithosphere (e.g. Ritter *et al.* 2001).

6.1 French Massif Central

In the French Massif Central, where the presence of a mantle plume has been suggested (e.g. Granet *et al.* 1995), melting, rifting and uplift episodes did not occur similarly in the northern and southern parts (e.g. Michon & Merle 2001). Although several studies support the mantle plume hypothesis, some other geodynamic events have been invoked to explain time delays (~ 15 Myr) between volcanic and sedimentation phases, as well as north–south differences in surface expression of the deep-seated thermal anomaly. Distinct mantle upwellings, or several upwelling phases (mantle pulses), could also partly explain the variability of geochemical signatures of magma sources. As emphasized in a recent review (Nehlig *et al.* 2003), geological and geophysical data related to volcanism and rifting in the French Massif Central are difficult to reconcile with present-day knowledge of a single geodynamic event. Nevertheless, our study shows new consequences for dynamic topography associated with a single mantle plume event. As an example, our results for the evolution of surface topography (e.g. Figs 6, 8a and b) show that plume-induced topographic variations can last more than 10 Myr. In the case shown in Fig. 8(b), a strongly asymmetric topography is obtained 5 Myr after plume head impingement at the base

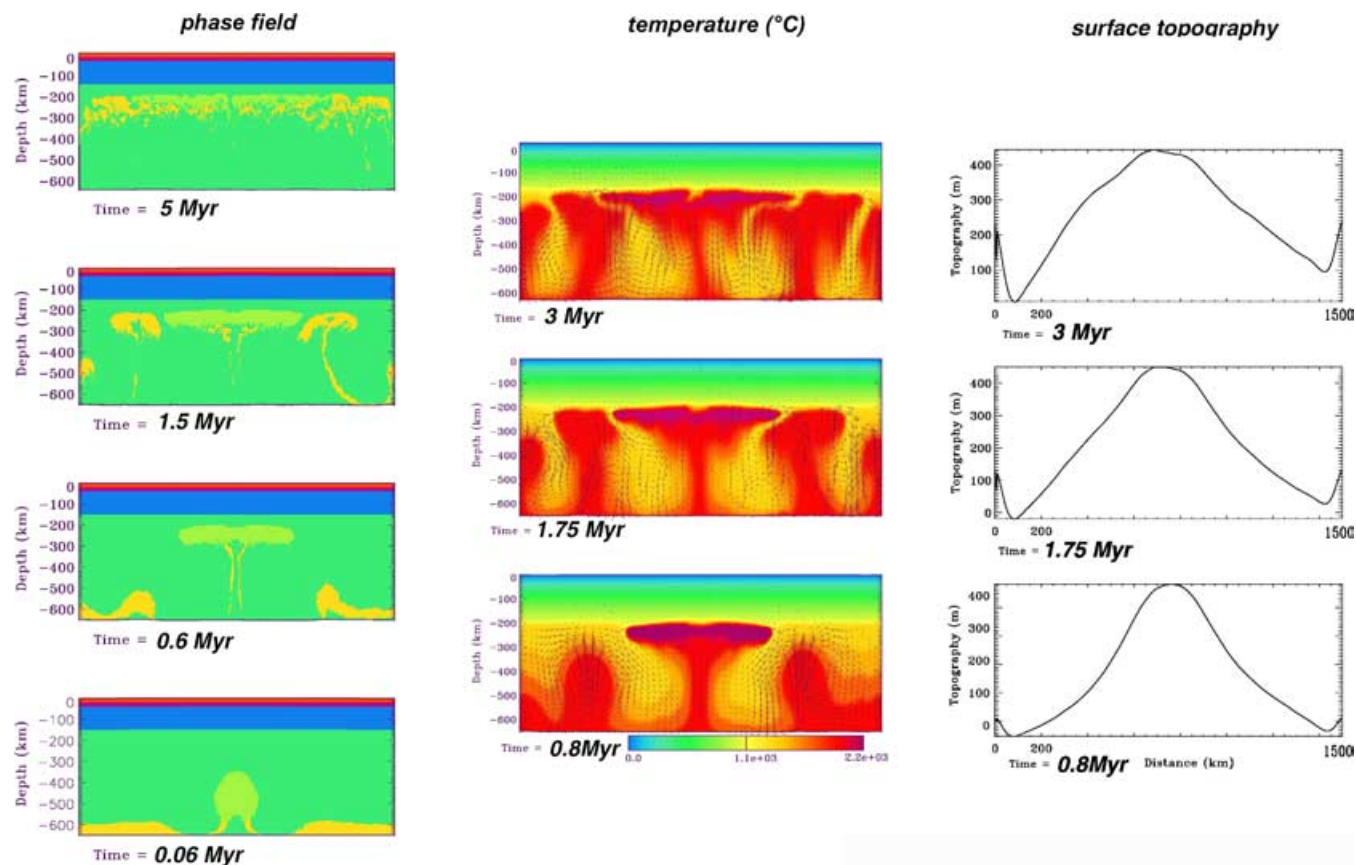


Figure 9. Experiments considering old (and cold, crust–mantle coupling) thick three-layer continental lithosphere (initial thermotectonic age 400 Ma; $Ra = 10^6$; background viscosity at depth $\mu \geq 10^{19}$ Pa s). $\Delta T = 250^\circ$ C. Initially old and cold lithosphere (400 Ma). Other notations are the same as for Fig. 7(a). For more detail, see colour pdf/html version of the paper.

of the continental lithosphere. Small-scale undulations (~ 50 km wide) progressively disappear while larger scale (~ 500 km) uplifts then dominate. In the French Massif Central, the Limagne basins (~ 40 km wide) appeared in the northern domain, approximately 10–15 Myr before the large domal signature (~ 400 km) that focused in the south.

6.2 East Africa

6.2.1 Mantle upwelling beneath east Africa

Several recent studies of the East African rift have pointed out seismic evidence for a deep thermal anomaly in the mantle, interpreted as dynamic signatures of a mantle plume (Ebinger & Sleep 1998; Nyblade *et al.* 2000; Davis *et al.* 2002; Weeraratne *et al.* 2003). As for the French Massif Central, many authors have attempted to explain the details of surface signatures with various scenarios of mantle upwellings. Instead of investigating the relevance of the present-day knowledge of the plume-induced topography, peculiar asthenospheric flow or original upwelling geometries have been suggested to explain geophysical and geochemical data from East Africa. For example, scattered volcanism, and the distribution and timing of uplift throughout East Africa have been explained by Ebinger & Sleep (1998) as resulting from lateral flow of plume material towards zones of thin lithosphere. George *et al.* (1998) have suggested two mantle plumes beneath Ethiopia in order to explain the 15-Myr time lapse between two distinct magmatic episodes. Ac-

cording to Davis *et al.* (2002), the East African rift results from three mantle currents impinging and eroding the base of the lithosphere. These mantle currents, which would result from separation of a deeper mantle upwelling, would have eroded the sphere, superimposing three dome-like structures on the overall uplift. Rather than explaining variations in surface signatures by complex upwelling geometries, it turns out from our results that improved numerical models of plume–lithosphere interaction can bring new ideas on the complex signatures resulting from a single subcontinental mantle plume. In the following, a detailed analysis of topographic signatures in East Africa is presented.

6.2.2 Spectral analysis of surface topography in east Africa

Our results have demonstrated that several topographic wavelengths can be induced by plume impingement at the base of the lithosphere. In East Africa, the three dome-like structures whose wavelengths are greater than 300 km are superimposed on the regional domal uplift of approximately 1500 km (Davis *et al.* 2002). These topographic signatures have been observed in several of our experiments (Figs 6 and 8). When smaller wavelengths are considered, field observations in the Northern Kenyan rift (Morley *et al.* 1992; Hendrie *et al.* 1994; Morley 1999) indicate that several rift basins, typically 30 km wide, were episodically active from the Oligocene to the Pliocene, while others were active for only a few million years. In the Turkana area, N Kenya and SW Ethiopia, faulting gradually shifted eastwards, and volcanism moved south and east with

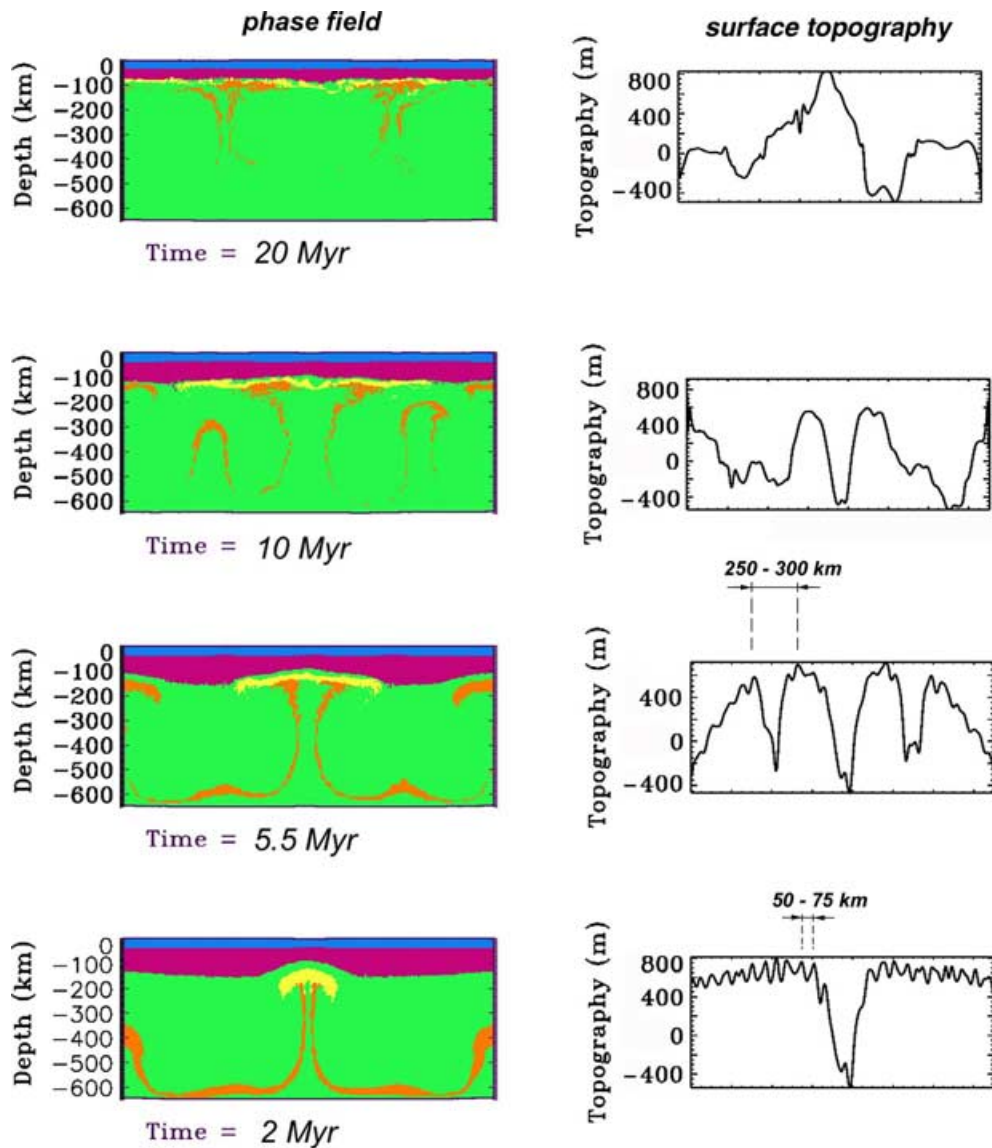


Figure 10. Effect of the plume head size on surface topography (phase field, left, and topography, right). All parameters are the same as in Fig. 7(a), but for plume head ($d = 100$ km) two times smaller. Note the presence of reduced wavelengths of surface deformation (50–75 km). For more detail, see colour pdf/html version of the paper.

time (Morley *et al.* 1992; Ebinger *et al.* 2000). Though spatial and temporal variations of uplift and subsidence signatures begin to be well documented (Morley 1999), a quantitative comparison with modelling results is not easy because, as we show in Section 5, the obtained surface signatures greatly depend on the thermal state and thickness of the lithosphere prior to plume ascent. Moreover, topographic variations of the lithosphere–asthenosphere boundary, which are not considered in this study, are expected to strongly affect asthenospheric flow (e.g. Ebinger & Sleep 1998). However, if the previously detailed physical principles, which describe the plume-induced topography, are proved to be valid, then several topographic wavelengths are supposed to be recorded at the surface, as sketched in Fig. 2(b). Thus, a spectral analysis of surface topography should provide new indicators of deep mantle processes.

A series of topographic profiles (global digital elevation model GTOPO30) from East Africa were selected in order to cover various areas where deep mantle upwellings have been suggested to occur, either presently or several tens of Ma. A rectangular grid was chosen

(26°E–43°E, 15°N–15°S) and east–west topographic profiles were analysed for each degree of latitude. Fig. 11 illustrates two profiles with their associated power spectrum density allowing for dominant wavelengths to be deciphered. In the case of the Main Ethiopian rift area (Fig. 11a), the spectrum clearly shows four distinct wavelengths. In the second case (Fig. 11b), three dominant wavelengths can be identified. Differences between these two spectra probably come from the distinct lithospheric structures encountered. In the second case, the Tanzania craton, which is supposed to represent a colder block (e.g. Nyblade *et al.* 2000; Petit & Ebinger 2000), probably affects the dynamic response of the lithosphere. Indeed, when dominant topographic wavelengths extracted from all profiles are combined (Fig. 12), this trend is confirmed from the northern to the southern edge of the craton. The major interesting point of this diagram is illustrated by the multimodal signature of the continental topography in response to mantle upwellings. In the Afar and Ethiopian areas, under which a mantle plume would be present, two dominant wavelengths appear at around 30–50 and 70 km. Two

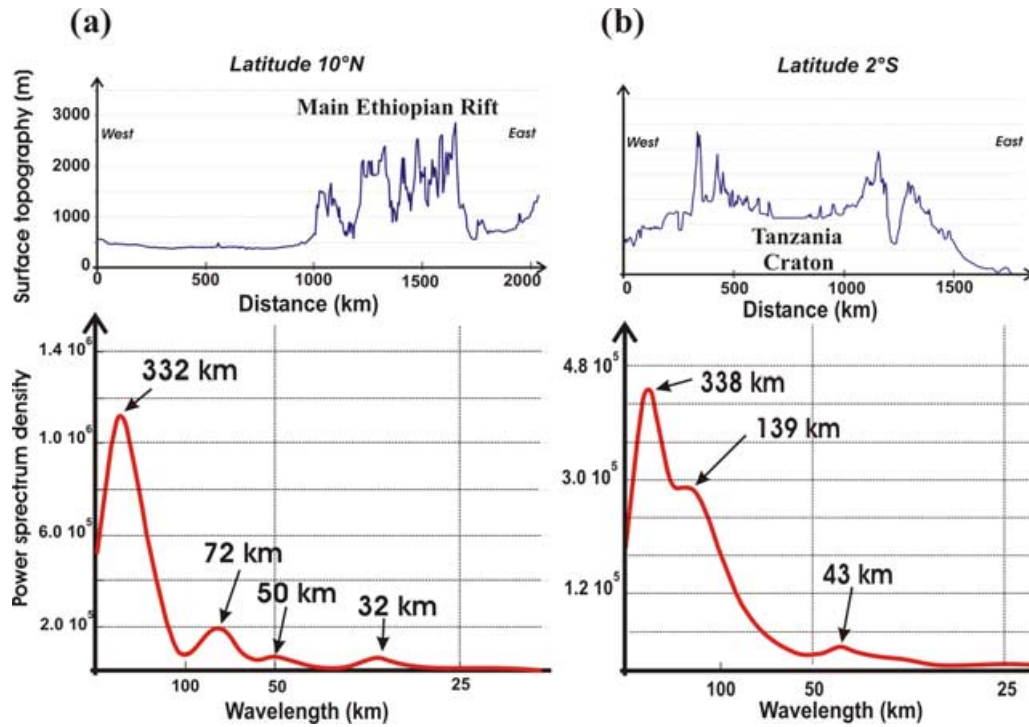


Figure 11. Surface topography profiles in east Africa and associated power spectral densities. (a) Latitude 10°N, corresponding to the Main Ethiopian rift area; (b) latitude 2°S, close to the published profile of Nyblade *et al.* (2000).

other distinct signatures peak at 330 and 390 km. In the south of the Tanzania craton (Malawi rift area), the smallest wavelengths are still present, whereas long wavelengths do not show a clear dichotomy. These two bimodal signatures at small and long wavelengths are probably the result of rheological layering of the continental lithosphere (crust and deep lithosphere), as it is explained in Fig. 2(b) and with our numerical results. Thermal state and rheological layering of the deep lithosphere probably differ between the north and the south of the Tanzania craton. The presence of intermediate wavelengths in the cratonic area may indicate a more complex rheological structure. However, if the cratonic lithosphere is rheologically homogeneous, the distinct intermediate wavelengths reported in Fig. 12 may reflect spatial differences in mantle flow.

6.2.3 Comparison with numerical results

In order to compare the spectral analysis with our numerical results, a similar procedure was employed to extract the dominant wavelengths of the numerical signatures. However, because large wavelengths are implicitly promoted by the numerical procedure, it is preferable to use the amplitude spectrum because the power spectrum density tends to attenuate short-wavelength components. Fig. 13 shows the smoothed amplitude spectrum of topographic profiles from Fig. 8(b). In that case, we sample four time steps in the plume–lithosphere interaction process, which is similar to a spatial sampling in East Africa. As it can be seen, each spectrum shows several distinct wavelengths. The values for long wavelengths are similar to those obtained in East Africa (from 284 to 395 km). Similarly, short wavelengths of 60–77 km are discriminated for each time step. Temporal variation of wavelength values may be considered as a spatial variation in a 3-D model. With such an analogy, one can mention that no dominant wavelengths are observed between 150

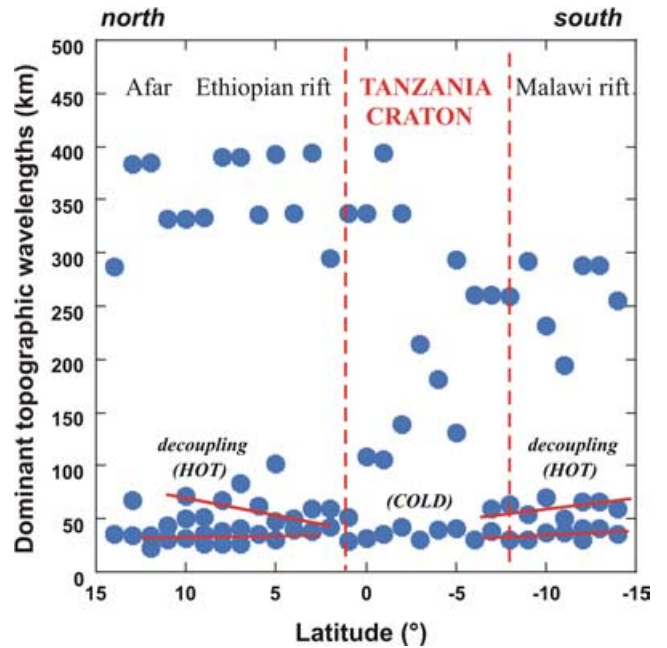


Figure 12. Spatial distribution of dominant topographic wavelengths, analysed from 31 east–west topographic profiles such as those in Fig. 11. The bimodal signatures at short and large wavelengths, and the possible influence of the Tanzania craton are discussed in the text.

and 284 km, as was observed for the northern part of east Africa (Fig. 12, Afar and Ethiopian areas).

A more complete comparison between real surface topography and models would not necessarily bring additional results. In particular, as a result of its limited resolution, the model includes flexural uplifts caused only by large fault displacements whereas the real

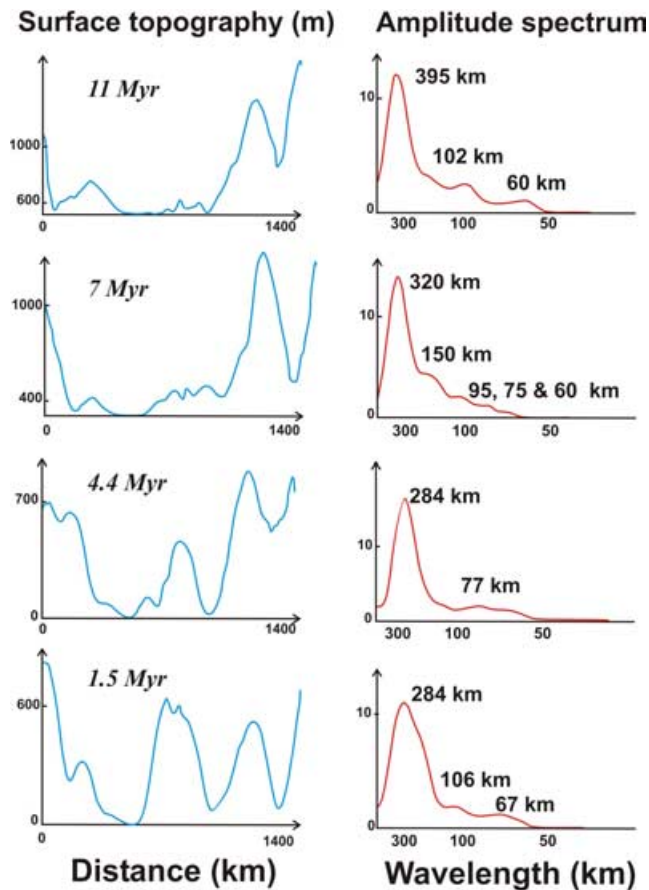


Figure 13. Same analysis as Fig. 11 for modelled topography of Fig. 8(b). Spatial and temporal evolution of dominant wavelengths are detailed in the text.

topography is also affected by intermediate- and small-scale faulting. Moreover, one must bear in mind that the modelled lithosphere does not possess lateral heterogeneities (thick cratons or thinned zones), in contrast to the African lithosphere. Absolute values of dominant wavelengths (real and modelled) cannot be compared quantitatively for obvious reasons (2-D profiles, erosion ...), but basic features (bimodal signatures, a gap between crustal and lithospheric wavelengths) must be considered as a reliable indicator of plume–lithosphere interaction. However, our analyses can help guide studies of plume–lithosphere interaction beneath East Africa.

Fig. 8(b) corresponds to a larger plume Rayleigh number (Ra_p) than the model of Fig. 8(a), where surface topography exhibits smoother undulations. Topographic profiles in East Africa clearly approach those of Fig. 8(b), allowing us to justify the possibility for large plume Rayleigh numbers, at least beneath east Africa.

6.3 Pannonian basin

The Pannonian basin is an area of pronounced lithospheric weakness since Cretaceous times with a high degree of strain localization (e.g. Cloetingh *et al.* 2002). The stretching and subsidence history of the Pannonian basin, the temporal and spatial evolution of the flexure of the Carpathian lithosphere, and the lithospheric strength of the region reflect a complicated early Miocene–to–present history of this segment of the Eurasia–Africa collision zone (Cloetingh *et al.* 2002, 2004). A number of key features of the Pannonian–Carpathian system resemble the experiments of Figs 8(b) and 10: (i) polyphase

evolution, (ii) formation of alternating internal sub-basins spaced at 200–300 km, and (iii) the simultaneous occurrence of climax of extension in the Pannonian basin and climax of compression in the surrounding Carpathian belt. It is possible that the evolution of this system is conditioned by mantle lithosphere instabilities caused by plume–lithosphere interaction both below the stretched Alpine pre-rift orogenic belt and the borders of the Eastern European platform. This scenario would be consistent with anomalous mantle lithosphere thinning in the Pannonian basin, and is compatible with inferences from seismic tomography demonstrating pronounced heterogeneity in the upper mantle under the Pannonian–Carpathian system, with stratification displaying pronounced lateral variations in contrast at the transition between East European platform/Moesian plate lithosphere and thinned lithosphere under the Pannonian basin.

7 CONCLUSION

Accounting for the free surface, EVP rheology and the positive buoyancy of continental crust provides a new understanding of possible tectonic and surface evolution resulting from plume–lithosphere interaction. In particular, the comparison with topography profiles from Europe and Africa provides quite encouraging first-order test of the models.

Mantle plumes interact with the continental lithosphere before manifesting themselves as complex topographic signatures. While oceanic lithosphere can be considered as a low frequency modulator, continental lithosphere behaves as a multifrequency modulator. The lithosphere may increase the largest plume-related wavelength at the expense of reduction in its amplitude. For this reason, continental plumes may not necessarily produce detectable large-scale topography, but instead easily detected alternating small- or middle-scale features normally attributed to regional tectonics. Attenuation of long surface wavelengths (>500 km) may occur in the case of weak, decoupled crust that accommodates the mantle uprise but negates its surface expression by thinning of upper layers (the degree of thinning is proportional for the degree of surface uplift).

In the case of decoupled rheology, the continental Moho presents a density and rheological barrier to propagation of plume material above or near Moho depths. The role of the competent mechanical core of the crust is as important as that of the mantle lithosphere (specifically in early Archean or recent lithosphere of <300 Ma age). Hence, crustal deformation may interfere with mantle deformation yielding complex periodic subsidence/uplift patterns. For example, surface evolution begins with a central uplift, but switches to subsidence accompanied by formation of adjacent basins. Both the amplitude and the wavelength of the EVP model with free surface differ from predictions of single-layer models with a fixed surface: the amplitudes of surface uplift are up to 2 times smaller; the initial regional wavelength of uplift is 20–30 per cent larger, there are also prominent secondary harmonics of deformation that correspond to small wavelengths (from 30–80 to 300–500 km), as identified in East Africa. The selection of discrete topographic wavelengths in response to plume–lithosphere interaction thus provides a new tool for inferring the most probable flow regime in the mantle.

In the case of strong lateral variation of plate thickness, impingement of the plume head produces both extension in the centre and compression at the far ends of the plate (eg. Fig. 10 at 5.5 Myr). Some concurrent extensional and compressional events, such as observed in the Pannonian–Carpathian system, may be explained by this effect. The lateral variations in plate thickness may result from the

impingement or from pre-existing tectonic evolution (plate boundaries).

We outline five important results, compared to the predictions of conventional viscous models.

(i) The appearance of additional short and intermediate wavelengths of deformation (alternating basins and uplifts), which do not correlate with the dimensions of the plume head; possible concurrent compression at the borders of the system may serve as an indicator of plume impact.

(ii) Poly-phase deformation related to progressive reduction of the resistance of lithospheric layers as the plume head flattens horizontally.

(iii) Reduced impact of plume ascent on the amplitude of long-wavelength surface elevations.

(iv) A concentration of plume-related extension in mantle lithosphere with little effect on decoupled crust; in the case of strong mechanical decoupling, the crust may not even feel the plume, which can be blocked below the Moho depth, although light residuals of partial melting may reach the surface.

(v) A modulation of the long-wavelength deformation.

ACKNOWLEDGMENTS

This is a Bureau de Recherches géologiques et Minières (BRGM) contribution 3359. We are grateful to Peter Molnar and Cindy Ebinger for critical reading and smoothing English of the revised version of the manuscript. C. Ebinger and two anonymous reviewers are also deeply thanked for their detailed and constructive comments that significantly helped to improve the manuscript. S. Cloetingh has pointed out the case of the Pannonian basin. The numerical code PAROVOZ V.9 is an outgrowth of PAROVOZ V.3 (1996) by Poliakov and Podladchikov (Poliakov *et al.* 1993). This study has benefited from partial support by Middle East Basin Evolution (MEBE) program.

REFERENCES

- d'Acremont, E., Leroy, S. & Burov, E.B., 2003. Numerical modelling of a mantle plume: the plume head–lithosphere interaction in the formation of an oceanic large igneous province, *Earth planet. Sci. Lett.*, **206**, 379–396.
- Anderson, D.L., 1982. Hotspots, polar wander, Mesozoic convection and the geoid, *Nature*, **297**, 391–393.
- Anderson, D.L., 1998. The scales of mantle convection, *Tectonophysics*, **284**, 1–17.
- Batchelor, G.K., 1967. *An introduction to fluid dynamics*, Cambridge Univ. Press, Cambridge, p. 615.
- Bauer, S.J. & Handin, J., 1983. Thermal expansion and cracking of three confined, water-saturated igneous rocks to 800° C, *Rock Mech. Rock Eng.*, **16**, 181–198.
- Bercovici, D., Ricard, Y. & Schubert, G., 2001. A two-phase model for compaction and damage 3. Applications to shear localization and plate boundary formation, *J. geophys. Res.*, **106**, 8925–8939.
- Burov, E.B. & Cloetingh, S., 1997. Erosion and rift dynamics: new thermo-mechanical aspects of post-rift evolution of extensional basins, *Earth planet. Sci. Lett.*, **150**, 7–26.
- Burov, E.B. & Diamant, M., 1995. The effective elastic thickness (T_e) of continental lithosphere: What does it really mean?, *J. geophys. Res.*, **100**, 3905–3927.
- Burov, E.B. & Poliakov, A.N.B., 2001. Erosion and rheology controls on synrift and postrift evolution: Verifying old and new ideas using a fully coupled numerical model, *J. geophys. Res.*, **106**, 16 461–16 481.
- Burov, E.B., Jolivet, L., Le Pourhiet, L. & Poliakov, A.N.B., 2001. A thermo-mechanical model of exhumation of high pressure (HP) and ultra-high pressure (UHP) metamorphic rocks in alpine-type collision belts, *Tectonophysics*, **342**, 113–136.
- Burov, E.B., Jaupart, C. & Guillou-Frotier, L., 2003. Ascent and emplacement of magma reservoirs in brittle-ductile upper crust, *J. geophys. Res.*, **108**, 2177, doi: 10.1029/2002JB001904
- Byerlee, J., 1978. Rock friction and earthquake prediction, *Pure appl. Geophys.*, **116**, 615–626.
- Canright, D. & Morris, S., 1993. Buoyant instability of a viscous film over a passive fluid, *J. Fluid. Mech.*, **255**, 349–372.
- Carter, N.L. & Tsenn, M.C., 1987. Flow properties of continental lithosphere, *Tectonophysics*, **36**, 27–63.
- Chapman, C.J., Childress, S. & Proctor, M.R.E., 1980. Long wavelength thermal convection between non-conducting boundaries, *Earth planet. Sci. Lett.*, **51**, 362–369.
- Cloetingh, S., Horváth, F., Bada, G. & Lankreijer, A., 2002. Neotectonics and surface processes: the Pannonian basin and Alpine/Carpathian system, *EGU St. Mueller Special Publication Series*, **3**, pp. 301.
- Cloetingh, S., Bada, G., Manco, L., Lankreijer, A., Horváth, F. & Dinu, C., 2004. Thermo-mechanical modelling of the Pannonian-Carpathian system: Modes of tectonic deformation, lithospheric strength and vertical motions, *Tectonics*, submitted.
- Condie, K.C., 2002. Continental growth during a 1.9-Ga superplume event, *J. Geodyn.*, **34**, 249–264.
- Condie, K.C., Des Marais, D.J. & Abbott, D., 2000. Geologic evidence for a mantle superplume event at 1.9 Ga, *Geochem. Geophys. Geosyst.*, **1**, paper no. 2000GC000095.
- Cooper, H.W. & Simmons, G., 1977. The effect of cracks on the thermal expansion of rocks, *Earth planet. Sci. Lett.*, **36**, 404–412.
- Courtillot, V., Jaupart, C., Manighetti, I., Tapponnier, P. & Besse J., 1999. On causal links between flood basalts and continental break-up, *Earth planet. Sci. Lett.*, **166**, 177–195.
- Craig, C.H. & McKenzie, D.P., 1986. The Existence of a Thin Low Viscosity layer beneath the lithosphere, *Earth planet. Sci. Lett.*, **78**, 420–426.
- Cserepes, L., Christensen, U.R. & Ribe, N.M., 2000. Geoid height versus topography for a plume model of the Hawaiian swell, *Earth planet. Sci. Lett.*, **178**, 29–38.
- Cundall, P.A., 1989. Numerical experiments on localization in frictional materials, *Ing. Arch.*, **59**, 148–159.
- Davies, G.F., 1992. Temporal variation of the Hawaiian plume flux, *Earth planet. Sci. Lett.*, **113**, 277–286.
- Davies, G.F., 1993. Cooling the core and mantle by plumes and plate flows, *Geophys. J. Int.*, **115**, 132–146.
- Davies, G. F., 1994. Thermomechanical erosion of the lithosphere by mantle plumes, *J. geophys. Res.*, **99**, 15 709–15 722.
- Davis, P.M. & Slack, P.D., 2002. The uppermost mantle beneath the Kenya dome and relation to melting, rifting and uplift in East Africa, *Geophys. Res. Lett.*, **29**, doi: 10.1029/2001GL013676
- Doin, M.-P., Fleitout, L. & Christensen, U., 1997. Mantle convection and stability of depleted and undepleted continental lithosphere, *J. geophys. Res.*, **102**, 2771–2787.
- Ebinger, C. & Sleep, N., 1998. Cenozoic magmatism in central and east Africa resulting from impact of a one large plume, *Nature*, **395**, 788–791.
- Ebinger, C.J., Yemane, T., Harding, D.J., Tesfaye, S., Kelley, S. & Rex, D.C., 2000. Rift deflection, migration, and propagation: Linkage of the Ethiopian and Eastern rifts, Africa, *Bull. geol. Soc. Am.*, **112**, 163–176.
- Farnetani, C.G. & Richards, M.A., 1994. Numerical investigations of the mantle plume initiation model for flood basalt events, *J. geophys. Res.*, **99**, 13 813–13 833.
- Foulger, G., 2002. Plumes, or plate tectonic processes?, *Astron. Geophys.*, **43**, 619–623.
- Frederiksen, S. & Braun, J., 2001. Numerical modelling of strain localisation during extension of the continental lithosphere, *Earth planet. Sci. Lett.*, **188**, 241–251.
- George, R., Rogers, N. & Kelley, S., 1998. Earliest magmatism in Ethiopia: evidence for two mantle plumes in one flood basalt province, *Geology*, **26**, 923–926.

- Gerbault, M., Poliakov, A.N.B. & Daignières, M., 1998. Prediction of faulting from the theories of elasticity and plasticity; what are the limits?, *J. Struct. Geol.*, **20**, 301–320.
- Goetze, C. & Evans, B., 1979. Stress and temperature in the bending lithosphere as constrained by ex-perimental rock mechanics, *Geophys. J. R. astr. Soc.*, **59**, 463–478.
- Granet, M., Wilson, M. & Achauer, U., 1995. Imaging a mantle plume beneath the French Massif Central, *Earth planet. Sci. Lett.*, **136**, 281–296.
- Griffiths, R.W. & Campbell, I.H., 1990. Stirring and structure in mantle plumes, *Earth planet. Sci. Lett.*, **99**, 66–78.
- Guillou, L. & Jaupart, C., 1995. On the effects of continents on mantle convection, *J. geophys. Res.*, **100**, 24217–24238.
- Hendrie, D.B., Kusznir, N.J., Morley, C.K. & Ebinger, C.J., 1994. Cenozoic extension in northern Kenya - a quantitative model of rift basin development in the Turkana region, *Tectonophysics*, **236**(1–4), 409–438.
- Houseman, G. & McKenzie, D.P., 1982. onset of convective instability in the Earth's mantle, *Geophys. J. R. astr. Soc.*, **68**, 133–164.
- Hunt, G., Muhlhaus, H., Hobbs, B. & Ord, A., 1996. Localized folding of viscoelastic layers, *Geol. Rundsh.*, **85**, 58–64.
- Ingle, S. & Coffin, M.F., 2004. Impact origin for the greater Ontong Java plateau?, *Earth planet. Sci. Lett.*, **218**, 123–134.
- Jellinek, M.A. & Manga, M., 2004. Links between long-lived hotspots, mantle plumes, D' and plate tectonics, *Rev. Geophys.*, **42**, 3, RG3003.
- Kiefer, W.S. & Hager, B.H., 1992. Geoid Anomalies and Dynamic Topography from Convection in Cylindrical Geometry: Applications to Mantle Plumes on Earth and Venus, *Geophys. J. Int.*, **108**, 198–214.
- Kirby, S.H. & Kronenberg, A.K., 1987. Rheology of the lithosphere: selected topics, *Rev. Geophys.*, **25**, 1219–1244.
- Kohlstedt, D.L., Evans, B. & Mackwell, S.J., 1995. Strength of the lithosphere: constraints imposed by laboratory experiments, *J. geophys. Res.*, **100**, 17 587–17 602.
- Kukkonen, I.T. & Peltonen, P., 1999. Xenolith-controlled geotherm for the central Fennoscandian Shield: implications for lithosphere-asthenosphere relations, *Tectonophysics*, **304**, 301–315.
- Lenardic, A., Guillou-Frottier, L., Mareschal, J.-C., Jaupart, C., Moresi, L.-N. & Kaula, W.M., 2000. What the mantle sees: the effects of continents on mantle heat flow, *Am. geophys. Un. Monogr.*, **121**, 95–112.
- Loper, D.E. & Stacey, F.D., 1983. The dynamical and thermal structure of deep mantle plumes, *Phys., Earth planet. Int.*, **33**, 304–317.
- McCulloch, M.T. & Bennett, V.C., 1994. Progressive growth of the Earth's continental crust and depleted mantle: geochemical constraints, *Geochim. cosmochim. Acta*, **58**, 4717–4738.
- Manglik, A. & Christensen, U.R., 1997. Effect of mantle depletion buoyancy on plume flow and melting beneath a stationary plate, *J. geophys. Res.*, **102**, 5019–5028.
- Mareschal, J.-C., Jaupart, C., Cheng, L.Z., Rolandone, F., Gariépy, C., Bienfait, G., Guillou-Frottier, L. & Lapointe, R., 1999. Heat flow in the Trans-Hudson Orogen of the Canadian Shield: implications for Proterozoic continental growth, *J. geophys. Res.*, **104**, 29 007–29 024.
- Michon, L. & Merle, O., 2001. The evolution of the Massif Central rift : spatio-temporal distribution of the volcanism, *Bull. Soc. Geol., Fr.*, **172**(2), 69–80.
- Molnar, P. & Jones, G.H., 2004. A test of laboratory based rheological parameters of olivine from an analysis of late Cenozoic convective removal of mantle lithosphere beneath the Sierra Nevada, California, USA, *Geophys. J. Int.*, **156**, 555–564.
- Monnereau, M., Rabinowicz, M. & Arquis, E., 1993. Mechanical erosion and reheating of the lithosphere: a numerical model for hotspot swells, *J. geophys. Res.*, **98**, 809–823.
- Montelli, R., Nolet, G., Dahlen, F.A., Masters, G., Engdahl, E.R. & Hung, S.H., 2004. Finite-frequency tomography reveals a variety of plume in the mantle, *Science*, **303**, 338–343.
- Morley, C.K., 1999. Basin evolution trends in East Africa, in *Geoscience of Rift Systems—Evolution of East Africa*, AAPG Studies in Geology n°44, pp. 131–150, ed. C.K. Morley, AAPG, Tulsa.
- Morley, C.K., Wescott, W.A., Stone, D.M., Harper, R.M., Wigger, S.T. & Karanja, F.M., 1992. Tectonic evolution of the northern Kenyan rift, *J. geol. Soc. Lond.*, **149**, 333–348.
- Nehlig, P., Boivin, P., de Goër, A., Mergoil, J., Prouteau, G., Sustrac, G. & Thiéblemont, D., 2003. Les volcans du Massif Central, *Geologues*, **130–131**, 66–91.
- Nyblade, A.A., Owens, T.J., Gurrillo, H., Ritsema, J. & Langston, C.A., 2000. Seismic evidence for a deep mantle thermal anomaly beneath east Africa, *Geology*, **28**, 599–602.
- Olson, P., 1990. Hotspots, swells and mantle plumes, in *Magma transport and storage*, pp. 33–51, ed. Ryan, M.P., Wiley, Chichester.
- Parsons, B. & Sclater, J.G., 1977. An analysis of the variation of ocean floor bathymetry and heat flow with age, *J. geophys. Res.*, **82**, 803–827.
- Perry, H.C. & Jaupart, C., 2004. Particular mantle dynamics induced by continental roots, *EOS, Trans. Am. geophys. Un.*, **85**(17), Joint Assembly supplement, abstract T41C-04.
- Petit, C. & Ebinger, C., 2000. Flexure and mechanical behavior of cratonic lithosphere: Gravity models of the East African and Baikal rifts, *J. geophys. Res.*, **105**, 19 151–19 162.
- Poliakov, A.N.B., Cundall, P., Podladchikov, Y. & Lyakhovskiy, V., 1993. An explicit inertial method for the simulation of visco-elastic flow: an evaluation of elastic effects on diapiric flow in two- or three-layers models, in *Flow and creep in the solar system: observations, modelling and theory*, pp. 175–195, eds Stone, D.B. & Runcorn, S.K., Kluwer, Dordrecht.
- Ranalli, G., 1995. *Rheology of the Earth*, 2nd edn, Chapman and Hall, London, p. 413.
- Ribe, N.M. & Christensen, U.R., 1994. Three-dimensional modeling of plume–lithosphere interaction, *J. geophys. Res.*, **99**, 669–682.
- Ritter, J.R.R., Jordan, M., Christensen, U.R. & Aschauer, U., 2001. A mantle plume below the Eifel volcanic fields, Germany, *Earth planet. Sci. Lett.*, **186**, 7–14.
- Schubert, G., Turcotte, D.L. & Olson, P., 2001. *Mantle convection in the Earth and planets*, Cambridge Univ. Press, Cambridge, p. 956.
- Sheth, H.C., 1999. Flood basalts and large igneous provinces from deep mantle plumes: fact, fiction, and fallacy, *Tectonophysics*, **311**, 1–29.
- Sleep, N., 1997. Lateral flow and ponding of starting plume material, *J. geophys. Res.*, **102**, 10 001–10 012.
- Sleep, N., 2002. Local lithospheric relief associated with fracture zones and ponded plume material, *Geochem. Geophys. Geosyst.*, **3**(12), 8506, doi: 10.1029/2002/2002GC00376.
- Sleep, N., 2003. Survival of Archean cratonic lithosphere, *J. geophys. Res.*, **108**, 2302, doi:10.1029/2001JB000169.
- Sleep, N., 2004. Thermal haloes around plume tails, *Geophys. J. Int.*, **156**, 359–362.
- Smith, R.B., 1975. Unified Theory of the Onset of Folding, Boudinage and Mullion Structure, *Bull. geol. Soc. Am.*, **88**, 1601–1609.
- Solomatov, V.S., 2001. Grain size-dependent viscosity convection and the thermal evolution of the Earth, *Earth planet. Sci. Lett.*, **191**, 203–212.
- Solomatov, V.S. & Moresi, L.-N., 1996. Stagnant lid convection on Venus, *J. geophys. Res.*, **101**, 4737–4753.
- Solomatov, V.S. & Moresi, L.N., 2000. Scaling of time-dependent stagnant lid convection; application to small-scale convection on Earth and other terrestrial planets, *J. geophys. Res.*, **105**, 21 795–21 817.
- Tackley, P.J., 2000. Mantle convection and plate tectonics; toward an integrated physical and chemical theory, *Science*, **288**, 2002–2007.
- Turcotte, D.L. & Schubert, G., 2002. *Geodynamics, applications of Continuum Physics to Geological Problems*, 2nd edn, Cambridge Univ. Press, Cambridge, p. 456.
- Van Keken, P., 1997. Evolution of starting mantle plumes: a comparison between numerical and laboratory models, *Earth planet. Sci. Lett.*, **148**, 1–11.
- Weeraratne, D.S., Forsyth, D.W., Fisher, K.M. & Nyblade, A.A., 2003. Evidence for an upper mantle plume beneath the Tanzanian craton from Rayleigh wave tomography, *J. geophys. Res.*, **108**, 2427, doi:10.1029/2002JB002273.
- Weinberg, R.F. & Podladchikov, Y., 1994. Diapiric ascent of magmas through power law crust and mantle, *J. geophys. Res.*, **99**, 9543–9559.

APPENDIX A: NUMERICAL MODEL

A1 Basic equations

The PAROVOZ is 2.5-D FLAC-type code (Cundall 1989; Poliakov *et al.* 1993). It is a mixed finite-difference/finite-volume element numerical scheme, in which the coordinate frame is Cartesian 2-D, but stress/strain relations are computed in full 3-D formulation. The Lagrangian mesh of PAROVOZ is composed of quadrilateral elements subdivided onto two couples of triangular subelements with trilinear shape functions. PAROVOZ is a large strain fully explicit time-marching algorithm. It locally solves full Newtonian equations of motion in a continuum mechanics approximation,

$$\langle \rho \ddot{\mathbf{u}} \rangle - \text{div} \boldsymbol{\sigma} - \rho \mathbf{g} = 0, \quad (\text{A1})$$

coupled with constitutive equations (of practically any kind),

$$\frac{D\boldsymbol{\sigma}}{Dt} = F(\boldsymbol{\sigma}, \mathbf{u}, \dot{\mathbf{u}}, \nabla \dot{\mathbf{u}}, \dots T \dots), \quad (\text{A2})$$

and with equations of heat transfer (heat advection $\dot{\mathbf{u}} \nabla T$ in the eq. A3 below is solved separately):

$$\rho C_p \partial T / \partial t + \dot{\mathbf{u}} \nabla T - k \text{div}(\nabla T) - H_r = 0, \quad (\text{A3})$$

$$\rho = \rho_0 [1 - \alpha(T - T_0)] = 0. \quad (\text{A4})$$

Here, \mathbf{u} , $\boldsymbol{\sigma}$, \mathbf{g} , k are the respective terms for the displacement, stress, acceleration as a result of body forces and thermal conductivity. The overdots refer to time derivatives. The triangular brackets in eq. (A1) specify conditional use of the related term: in quasi-static mode inertial terms are dumped using inertial mass scaling (Cundall 1989). The terms t , ρ , C_p , T and H_r designate respectively time, density, specific heat, temperature and internal heat production. α designates the thermal expansion coefficient and the subscript 0 refers to the parameter value at the reference state. The terms $\partial/\partial t$, $D\boldsymbol{\sigma}/Dt$, F are a time derivative, an objective (Jaumann) stress time derivative and a functional, respectively. In the Lagrangian method, the incremental displacements are added to the grid coordinates allowing the mesh to move and deform with the material. This enables solution of large-strain problems locally using small-strain formulation: on each time step, the solution is obtained in local coordinates, which are then updated in the large strain mode.

Solution of eq. (A1) provides velocities at mesh points used for computation of element strains and of heat advection $\dot{\mathbf{u}} \nabla T$. These strains are used in eq. (A2) to calculate element stresses and the equivalent forces used to compute velocities for the next time step. As a result of the explicit approach, there are no convergence issues, which is rather a common problem of implicit methods in the case of non-linear rheologies.

A1.1 Large displacements and remeshing

The algorithm incorporates adoptive remeshing to handle large strains and large displacements, such as convective movements, within a Lagrangian framework. Remeshing is implemented when the mesh becomes too distorted, i.e. when the minimal angle of elements reaches a pre-defined value (here 8°). Remeshing is done by weighted linear interpolation of the nodal values (velocity, mass and temperature field) and of the barycentric values for triangles (stress, strain, material phases, accumulated strain, viscosities). The algorithm searches for barycentres of triangles from the old mesh and finds closest (by Hemming's criterion) barycentres from the new

mesh. Passive markers are used to improve the accuracy of interpolation. An additional interactive procedure is used to minimize phase diffusion so that mass balance for each phase is conserved.

A1.1.1 Stability

Dynamic time stepping is used: the algorithm automatically tests and adopts the internal time step using Courant's criterion for propagation of information (elastic waves, thermal diffusion), which allows one to provide a stable solution. Maxwell relaxation time for each time step is verified to insure that no stress relaxation occurs between two time steps. Reference experiments were repeated with 10 times smaller than Courant's/Maxwell limit on the time step.

A1.1.2 Pressure

Our approach has the advantage that it solves equations of motion for full stresses. It is thus of trivial matter to compute complete pressure p , which simply equals one-third of the trace of the full stress tensor ($\frac{1}{2} \sigma_{kk}$). The difference between complete pressure p and its lithostatic component $\rho g z$ equals dynamic pressure P .

A2 Explicit serial plastic–elastic–viscous rheology

We use a serial (Maxwell type) body (eq. 1), in which the total strain increment in each element is defined by a sum of elastic, viscous and brittle strain increments. Consequently, in contrast to fluid dynamic approaches, where non-viscous rheological terms are simulated using pseudo-plastic and pseudo-elastic viscous terms (e.g. Solomatov & Moresi 2000; Bercovici *et al.* 2001), our method treats all rheological terms explicitly. The parameters of elastic–ductile–plastic constitutive relationships for the crust and mantle come from rock mechanics data (Tables 1 and 2; Kirby & Kronenberg 1987; Kohlstedt *et al.* 1995).

A2.1 Plastic (brittle) behaviour

The brittle behaviour of rocks is described by Byerlee's law (Byerlee 1978; Ranalli 1995), which corresponds to non-associated (zero dilatation but finite friction angle) Mohr–Coulomb material with friction angle $\phi = 30^\circ$ and cohesion $|C_0| < 20$ MPa (e.g. Gerbault *et al.* 1998):

$$|\tau| = C_0 - \sigma_n \tan \phi, \quad (\text{A5})$$

where σ_n is normal stress $\sigma_n = \frac{1}{2} \sigma_1 + \sigma_{II}^{\text{dev}} \sin \phi$, $\frac{1}{2} \sigma_1 = P$ is the effective pressure, σ_{II}^{dev} is the second invariant of deviatoric stress, or effective shear stress. The condition of transition to brittle deformation (function of rupture f) reads as: $f = \sigma_{II}^{\text{dev}} + P \sin \phi - C_0 \cos \phi = 0$ and $\partial f / \partial t = 0$. In terms of principal stresses, the equivalent of the yield criterion (5) reads as:

$$\sigma_1 - \sigma_3 = -\sin \phi (\sigma_1 + \sigma_3 - 2C_0 / \tan \phi). \quad (\text{A6})$$

A2.2 Elastic behaviour

The elastic behaviour is described by linear Hooke's law:

$$\sigma_{ij} = \lambda \varepsilon_{ii} \delta_{ij} + 2G \varepsilon_{ij}, \quad (\text{A7})$$

where λ and G are Lamé's constants. Repeated indexes mean summation and δ is Kronecker's operator.

A2.3 Viscous (ductile) behaviour

Mantle convection and lithospheric deformation, including the lower crust, is controlled by thermally activated creep (Kirby & Kronenberg 1987; Ranalli 1995), which corresponds to a non-Newtonian power-law fluid:

$$e_{ij}^d = A(\sigma_1 - \sigma_3)^n \exp(-QR^{-1}T^{-1}), \quad (\text{A8})$$

where $e_{ij}^d = \dot{\epsilon}$ is the shear strain rate, A is material constant, n is power-law exponent, Q is activation enthalpy, R is Boltzman's gas constant and T is temperature in K, σ_1 and σ_3 are the principal stresses. The effective viscosity μ_{eff} for this law is defined as

$$\tau_{ij} \equiv \mu_{\text{eff}} e_{ij}^d, \quad (\text{A9})$$

which yields

$$\mu_{\text{eff}} = e_{ij}^{d(1-n)/n} A^{-1/n} \exp[Q(nRT)^{-1}]. \quad (\text{A10})$$

For non-uniaxial deformation, the law (A10) is converted to a triaxial form, using the invariant of strain rate and geometrical proportionality factors:

$$\mu_{\text{eff}} = e_{\text{II}}^{d(1-n)/n} (A^*)^{-1/n} \exp[Q(nRT)^{-1}],$$

where

$$e_{\text{II}}^d = [\text{Inv}_{\text{II}}(e_{ij})]^{1/2} \quad \text{and} \quad A^* = \frac{1}{2} A \times 3^{(n+1)/2}, \quad (\text{A11})$$

parameters A , n , Q are experimentally determined material constants (Table 2). Using olivine parameters (Table 2), one can verify that the predicted effective viscosity at the base of the lithosphere is 10^{19} – 5×10^{19} Pa s matching post-glacial rebound data (Turcotte & Schubert 2002). In the depth interval of 200–0 km, the effective viscosity grows from 10^{19} to 10^{25} – 10^{27} Pa s with decreasing temperature. Within the adiabatic temperature interval at depth, the dislocation flow law (A8) is replaced by nearly Newtonian diffusion creep, which results in quasi-constant mantle viscosity of 10^{19} – 10^{21} Pa s (e.g. Turcotte & Schubert 2002). Weinberg & Podladchikov (1994) have also shown that the effective viscosity in close vicinity of an ascending diapir is influenced by the local strain rate field and partly by heat exchanges between the diapir and surrounding rock, which suggests possible change in local creep mechanism.

APPENDIX B: THE PLUME ASCENT VELOCITY

The mechanics of plumes and diapirs was investigated in a number of studies using slightly different conceptual models (e.g. Weinberg & Podladchikov 1994 and references therein). Most theoretical mod-

els consider spherical diapirs whose ascent velocity v_s is given by solution of Stokes problem. Because this solution is obtained for an infinite space, the estimated ascent rates are applicable only to important depths. For simple Newtonian viscosity and translating isothermal spherical plumes, Stokes law provides an estimation for v_s determined from the ratio of buoyancy force f_a to the viscous drag force f_v [$f_a = \Delta\rho g(4/3\pi r^3)$, $f_v = 6\pi r\mu v_s$]. The ratio f_a/f_v should be > 1 to initiate ascent, which yields:

$$v_s = 2/9 \Delta\rho g r^2 \mu^{-1}, \quad (\text{B1})$$

where μ is the mean viscosity of the surrounding material, $\Delta\rho$ is the density contrast, g is the acceleration as a result of gravity, $r = 0.5D$ is the plume radius. The characteristic heat diffusion time is $t_d = r^2 \chi^{-1}$ and the ascent time is $t_a = (d-h)/v_s$, where χ is thermal diffusivity, d is the initial plume depth and h is its final depth below the lithosphere. One should require $t_d \gg t_a$ for plume ascent driven by thermal buoyancy. This corresponds to the definition of plume Rayleigh number $Ra_p > 1000$ (see eq. 5 in the text). The relation (B1) predicts low ascent rates of 0.2–0.5 m yr⁻¹. Temperature-dependent Newtonian viscosity provides higher but still not important ascent rates of approximately 1–2 m yr⁻¹. Accounting for non-Newtonian behaviour provides up to 1000 times higher ascent rates (Fig. 2a). According to Weinberg & Podladchikov (1994), in this case the effective dynamic viscosity μ_{eff} and the ascent rate can be estimated assuming characteristic buoyancy driven stress $\sigma = \Delta\rho g r$ (i.e. $f_a = \int_v \sigma dV$):

$$\partial\epsilon/\partial t = \sigma^n A \exp(-Q/RT), \quad (\text{B2})$$

$$\mu_{\text{eff}} = [6^{n-1} \exp(Q/RT)]/[3^{-(n-1)} A (\Delta\rho g r)^{n-1}], \quad (\text{B3})$$

$$v_y = \Delta\rho g r^2 / 3\mu_{\text{eff}} = 3^{-(n-1)} r A \times (\Delta\rho g r)^n / [3 \times 6^{n-1} \exp(Q/RT)], \quad (\text{B4})$$

where $\Delta\rho = \Delta\rho_{\text{ch}} + \alpha\rho_m \Delta T$, where $\Delta\rho_{\text{ch}}$ is the chemical density contrast with the embeddings and ρ_m is the reference density of the plume material, v_y is the ascent velocity, α is the coefficient of thermal expansion. ΔT is the temperature contrast with the embeddings. Assuming typical parameters (Tables 1 and 2), we obtain ascent rates as high as 10–5000 m yr⁻¹. The temperature and softening of the surrounding rock is conditioned by heat transfer from the plume, which is neglected in eq. (B4) that is valid for fast ascent without heat exchange. At the final ascent stage, heat loss becomes important because the ascent rate drops as a result of: (i) the free upper surface, (ii) increasing resistance of colder surrounding rocks, and (iii) decreasing chemical density contrast.